

1 **Going to Extremes: Installing the World's Highest Weather Stations on Mount Everest**

2 Matthews T. ^{1*}, Perry L.B. ², Koch I. ³, Aryal D. ⁴, Khadka A. ^{3,4}, Shrestha D. ⁴, Abernathy K. ⁵,

3 Elmore A.C. ⁵, Seimon A. ², Tait A. ⁵, Elvin S. ⁵, Tuladhar S. ⁶, Baidya S.K. ⁶, Potocki M. ⁷, Birkel

4 S.D. ⁷, Kang S. ^{8,9}, Sherpa T.C. ³, Gajurel A. ¹⁰, Mayewski P.A. ⁷

7 **Affiliations**

8 ¹ Department of Geography and Environment, Loughborough University, Loughborough, UK

9 ² Department of Geography and Planning, Appalachian State University, Boone, North Carolina,
10 USA

11 ³ International Centre for Integrated Mountain Development, Lalitpur, Nepal

12 ⁴ Central Department of Hydrology and Meteorology, Tribhuvan University, Kathmandu, Nepal

13 ⁵ National Geographic Society, 1145 17th St., Washington, D.C., USA

14 ⁶ Department of Hydrology and Meteorology, Kathmandu, Nepal

15 ⁷ Climate Change Institute, University of Maine, Orono, Maine, USA

16 ⁸ State Key Laboratory of Cryospheric Science, Northwest Institute of Eco-Environment and
17 Resources, Chinese Academy of Sciences (CAS), Lanzhou, China

18 ⁹ CAS Center for Excellence in Tibetan Plateau Earth Sciences, Beijing, China

19 ¹⁰ Central Department of Geology, Tribhuvan University, Kathmandu, Nepal ***Corresponding**

20 **Author.** Additional contact details (address given as affiliation 1): e-mail:

21 t.matthews@lboro.ac.uk; phone: 00441509222788

22

Early Online Release: This preliminary version has been accepted for publication in *Bulletin of the American Meteorological Society*, may be fully cited, and has been assigned DOI 10.1175/BAMS-D-19-0198.1. The final typeset copyedited article will replace the EOR at the above DOI when it is published.

23 **Abstract**

24 As the highest mountain on Earth, Mount Everest is an iconic peak that offers an unrivalled
25 natural platform for measuring ongoing climate change across the full elevation range of Asia's
26 water towers. However, Everest's extreme environment challenges data collection, particularly
27 on the mountain's upper slopes, where glaciers accumulate mass and mountaineers are most
28 exposed. Weather stations have operated on Everest before, including the world's previous
29 highest, but coverage has been sparse in space and time. Here we describe the installation of a
30 network of five automatic weather stations (AWSs), including the two highest stations on Earth
31 (8,430 m.a.s.l and 7,945 m.a.s.l) which greatly improves monitoring of this iconic mountain.
32 We highlight sample applications of the new data, including an initial assessment of surface
33 energy fluxes at Camp II (6,464 m.a.s.l) and the South Col (7,945 m.a.s.l), which suggest melt
34 occurs at both sites, despite persistently below-freezing air temperatures. This analysis
35 indicates that melt may even be possible at the 8,850 m.a.s.l summit, and prompts a re-
36 evaluation of empirical temperature index models used to simulate glacier melt in the Himalaya
37 that focus only on air temperature. We also provide the first evaluation of numerical weather
38 forecasts at almost 8,000 m.a.s.l and use of model output statistics to reduce forecast error,
39 showcasing an important opportunity to improve climber safety on Everest. Looking forward,
40 we emphasize the considerable potential of these freely available data for understanding
41 weather and climate in the Himalaya and beyond, including tracking the behavior of upper-
42 atmosphere winds, which the AWS network is uniquely positioned to monitor.

43

44 **Capsule**

45 We installed the world's highest weather stations on Mount Everest, offering new insights into
46 water resources under climate change, and potentially improving climber safety.

47

48 **Introduction**

49 Mountains cover 25% of the Earth's land surface and their snow and ice stores act as water
50 towers for more than a billion people worldwide (Immerzeel et al., 2019, 2010; Meybeck et al.,
51 2001; Viviroli et al., 2007). They are locations of especially hazardous weather extremes
52 (Moore and Semple, 2006; Wang et al., 2015), and a natural observation platform from which
53 to observe globally-significant high-altitude winds (Abish et al., 2015; Moore and Semple,
54 2004). The climate is also warming at altitude more rapidly than the global mean, which makes
55 these water towers vulnerable to accelerated melt (Mountain Research Initiative EDW Working
56 Group et al., 2015). It is unfortunate, then, that continuous observations from automatic
57 weather stations (AWSs) are biased toward lower, more accessible elevations (Figure 1). The
58 problem is particularly apparent in High Mountain Asia (HMA), where only a handful of AWSs
59 have been installed above 5,000 m.a.s.l, an elevation above which almost 62,000 km² of glacier
60 area in HMA is located (around 63% of the total HMA glacierized area); above 6,000 m.a.s.l
61 nearly 11,000 km² (around 11% of the glacierized area) is found, yet we were unaware of a
62 single AWS in HMA still operating above this elevation when our project started (observations
63 from 6,352 m.a.s.l on Nepal's Mera Peak ceased in November, 2016).

64 Perhaps the most ambitious prior effort to fill the high-altitude observational gap was
65 by the Ev-K2-CNR Committee (Locci et al., 2014) which, beginning in 1993, established a
66 network of six AWSs from 2,660 m.a.s.l to almost 8,000 m.a.s.l on the Nepalese side of Everest
67 (also known in local languages as Sagarmatha or Qomolangma), and included the world's
68 highest AWS at Everest's South Col (Bertolani et al., 2000; Salerno et al., 2015). That network
69 has provided valuable insights, including the assessment of dangerous weather events high on
70 Everest (Moore and Semple, 2011), and the identification of emerging climate trends (Salerno
71 et al., 2015). It has also been used to help drive glacier mass balance models (Shea et al., 2015).
72 However, the quality and number of observations from the AWSs is reduced at higher

73 elevations, with the South Col record particularly short and fragmentary. The Ev-K2-CNR
74 installation there was performed by a team of Italians and Nepalis in May 2008 (Moore et al.,
75 2012a), building on previous, very short-term deployments by North American researchers in
76 both 1996 (Lau, 1998) and 1998 (Moore and Semple, 2004). Air temperature data were
77 available intermittently from the Ev-K2-CNR South Col station until 2011, when the AWS was
78 apparently destroyed by wind-blown debris, highlighting the extremely challenging
79 environment for prolonged data collection (Verza, *pers. comm*). Since 2011, the highest AWSs
80 installed in the Khumbu region were on Kala Patthar summit and Changri Nup Glacier, at
81 altitudes of 5,600 and 5,700 m.a.s.l, respectively (Locci et al., 2014; Salerno et al., 2015). On
82 the Chinese (north) side of Everest, AWSs have been deployed at the North Col (7,028 m.a.s.l)
83 and the Ruopula Pass (6,560 m.a.s.l) (Yang et al., 2011), but they have not been active since
84 2008 and 2010, respectively.

85 There are very strong scientific and human safety motivations to establish a new
86 network of AWSs high on Everest. First, around 20% of the surface area, and almost all of the
87 accumulation zones of the glaciers in the Dudh Koshi River basin (within which the Khumbu
88 region is located) are situated above 5,800 m.a.s.l (Salerno et al., 2015; Shea et al., 2015),
89 meaning there is currently no in-situ monitoring of climate variables at elevations critical for
90 regional water-resource monitoring. Second, the extreme altitude enables direct and continuous
91 monitoring of the jet stream winds -- globally significant circulation features that may be
92 changing in strength and location as the climate warms (Abish et al., 2015). Third, climbers
93 continue to attempt to summit Everest in growing numbers, and deterioration in the weather is
94 a major contributor to death rates high on the mountain (Firth et al., 2008), where weather
95 observations are absent and the performance of forecasts unknown.

96 Considering these motivations, we undertook an ambitious program to install a network
97 of five AWSs during the pre-monsoon climbing season of 2019 as part of the National

98 Geographic and Rolex Perpetual Planet Expedition to Mt. Everest (hereafter 2019 Everest
99 Expedition). This effort was spearheaded by the meteorology team on what was an ambitious
100 multidisciplinary expedition that also included glaciology, biology, geology, and mapping
101 components (National Geographic, 2019). In what follows, we describe the installation of this
102 network, including the design specification of the stations for the extreme environment. We
103 then show preliminary data collected by the network and highlight their utility in addressing
104 some of the motivations explained above. We close by highlighting potential avenues for future
105 research utilizing this new, freely available data source.

106 **Network Design**

107 *Site Selection*

108 To improve weather monitoring in the Khumbu region, the 2019 Everest Expedition planned
109 not only to extend the measurement network to new heights, but also to improve the density
110 and quality of observations at lower elevations. At present, a lack of basic hydro-
111 meteorological observations in the region inhibits understanding of evolving water resources
112 under climate change (Krishnan et al., 2019; You et al., 2017). We aimed to help fill this gap
113 by installing AWSs that monitor liquid and solid precipitation and snow depth and variables
114 required to resolve the surface energy fluxes (Wild et al., 2017; Table 1).

115 Five potential sites for AWS deployments were selected based on the following: (1) the
116 anticipated utility of measurements from each location, and (2) the logistical challenges of
117 installation and longer-term maintenance (Figure 2). The lowest of these sites, Phortse (3,810
118 m), was selected because its abundant flat ground and largely unobstructed sky provides an
119 excellent location for measuring radiation and precipitation (including a double-alter wind
120 shield). The Pumori Bench (5,315 m), a vegetated medial moraine close to Everest's Base
121 Camp, was chosen as the only other location below the Khumbu Ice Fall (a dangerous obstacle
122 to climbers). This site enables weather observations representative of the Khumbu Glacier's

123 upper, clean-ice ablation area (Rounce et al., 2018), an area of interest to glacier-climate studies
124 (Pratap et al., 2015). The Pumori Bench is also relatively stable, and therefore suitable for
125 precipitation sensors and a double-alter wind shield. Due to its proximity to such a well-known
126 location on the Everest climbing route, we refer to this station as “Base Camp” hereafter.

127 Above the Khumbu Ice Fall, we selected sites at Everest’s Camp II (~6,400 m.a.s.l),
128 the South Col (~7,900 m.a.s.l), and as close to Everest’s 8,850 m.a.s.l summit as possible. All
129 these locations are along the main southern Nepalese Everest climbing route, which maximizes
130 accessibility for maintenance visits. Camp II represents the approximate maximum elevation
131 of the 0°C isotherm in the Khumbu region according to Shea et al. (2015), and is therefore an
132 opportune site for tracking this important meteoric parameter for glacier mass balance (Bradley
133 et al., 2009; Carrasco et al., 2005). In the interests of data continuity, we aimed to install the
134 new South Col AWS on bedrock close to the previous Italian station. For the uppermost station
135 a number of possible sites were identified in appreciation of the challenges posed by journeying
136 to 8,850 m.a.s.l, including the “Balcony” (8,430 m.a.s.l), and South Summit (8,749 m.a.s.l).

137 *Design Specification*

138 A critical part of preparing the network was identifying the likely demands on the
139 highest AWSs from extreme weather. To guide us, we used ERA-Interim reanalysis data from
140 the European Centre for Medium Range Weather Forecasts (ECMWF; Dee et al., 2011),
141 interpolating six-hourly wind speeds and air temperatures from the closest model levels to the
142 latitude, longitude and elevation of the summit. These pre-fieldwork results indicated a
143 maximum wind speed of 76 m s^{-1} , and a minimum temperature of -49°C during 1979-2018
144 (Fig. 3). However, the former refers to means rather than instantaneous gusts, so we multiplied
145 by 1.4 (a representative gust factor for strong winds in mountainous terrain: Ágústsson and
146 Ólafsson, 2004) to obtain a precautionary estimate of extreme winds. This scaling updated the
147 maximum wind speed to around 106 m s^{-1} which, if reached, would surpass the world record

148 outside a tropical cyclone or tornado (WMO, 2019). We took this as our design standard for
149 wind speed (for both the South Col and summit), and also ensured that the AWSs should be
150 resilient to temperatures of -60°C and an atmospheric pressure of 311 hPa (the minimum value
151 in the reanalysis data for the summit).

152 The AWSs were designed with Campbell Scientific, Inc. (from which the stations were
153 purchased) to cope with these extreme meteorological demands through a two-pronged
154 approach. First, some sensors for the two highest stations underwent special low-temperature
155 modifications, and battery-heaters and insulation were added to safeguard the power supply.
156 Telemetry and data logging programs were also designed to be robust and conserve power,
157 with double-redundant transmission (Thuraya satellite modem or radio transmission to Base
158 Camp AWS), and a high capacity micro-SD card in case transmission was paused due to low
159 power. The second means of ensuring resilience of the two highest AWSs was to guard against
160 the additional challenges of high wind and extreme low pressure. We did this by designing the
161 custom tripods to be guy-wired and bolted to bedrock and planned for redundant temperature
162 and wind speed sensors. We also subjected AWS sensors to a full system test in a low
163 temperature hypobaric chamber before deployment.

164 In addition to being robust, the summit and South Col AWSs had to be: 1) lightweight,
165 since they would be hand-carried to extreme elevations; and 2) require minimal setup time
166 (~1.5 hours) due to the extreme environmental conditions facing the climbing team (e.g. limited
167 supplementary oxygen, cold, fatigue). The total weight of each station was therefore limited to
168 ~50 kg (Table 1). To facilitate a quick installation while wearing gloves/mittens, the tripod,
169 cross arms, and all mounts were designed with twist knobs and/or pins with quick release
170 handles. All sensor cables were also pre-wired to a Campbell Scientific CR1000x data logger
171 inside an insulated Pelican case with military-specification quick-connect fittings (Fig. 2).

172 *Installation of the Weather Stations*

173 Our team installed the AWS network in April and May 2019. The Phortse, Base Camp and
174 Camp II deployments used conventional tripods and were relatively straightforward; however,
175 the two highest installations were considerably more complex given the extreme environmental
176 conditions and logistics of carrying two 50 kg AWSs up the ~1,500 m-high Lhotse Face (Fig.
177 2). After a regimented acclimatization schedule and many training deployments of these
178 custom AWSs, the team left Everest Base Camp on 18 May 2019 to install the uppermost
179 stations, climbing to the South Col over four days. We installed the new AWS there
180 approximately 30 m higher than the most recent EV-K2-CNR deployment (Salerno et al.,
181 2015), in an area farther from debris which could impact the station during periods of extreme
182 winds. The first observation from the South Col AWS was received at 1145 Nepal Time (NPT)
183 on 22 May 2019 indicating a temperature of -17.8°C , 53% relative humidity, 380 hPa pressure,
184 and winds out of the west-southwest at 8.5 m s^{-1} gusting to 15 m s^{-1} , resulting in a wind chill
185 of -29.8°C

186 The summit push began at 2300 NPT on 22 May 2019. Our team of 22, including 14
187 Sherpas, three scientists (Matthews, Perry, Potocki), three media team members, and two
188 Nepalese climbers, made substantial progress for the first three hours. A traffic jam of climbers
189 then slowed progress, consistent with the very narrow time window suitable for summitting
190 according to available weather forecasts (Wilkinson, 2019). Given the exceptionally slow pace
191 and visible crowding farther up the route, safety concerns prompted us to install our highest
192 AWS at the Balcony (the lowest targeted “summit” site), at around 0400 NPT.

193 The Balcony deployment was hindered by the extreme cold, with drill batteries
194 (required to set the rock anchors for the tripod) needing to be warmed by body heat to restore
195 their function. We also observed that the critical mounts for the wind sensors were missing, so
196 we improvised replacements using lightweight aluminium shovel handles approximately the
197 same diameter as the original pipe mounts (Fig. 2). The installation of the world’s first AWS

198 above 8,000 m.a.s.l was completed shortly before 0645 NPT on 23 May 2019, with initial
199 measurements of -23.9°C air temperature, 78% relative humidity, 355 hPa pressure, and winds
200 out of the northeast at 1.7 m s^{-1} gusting to 5.5 m s^{-1} , translating to a wind chill of -29.6°C .

201 *Initial Observations*

202 All except the Base Camp AWS¹ have been operating since the 2019 Everest Expedition and
203 we focus here on interesting aspects of the record up to 31 October 2019. The preliminary data
204 (Figure 4) highlight the considerable range of conditions spanned by the network in space and
205 time, with the Balcony site on average 28°C lower in air temperature than the Phortse site
206 (4,620 m below). Consistent with previous research we observe the temperature lapse rate to
207 exhibit strong seasonality, including a shift to shallower values during the monsoon (Immerzeel
208 et al., 2014; Kattel et al., 2013), which started around 1 July 2019. The decline in high altitude
209 winds, increase in relative humidity, and initiation of substantial precipitation accumulations
210 at Phortse, identify this monsoon onset and indicate a somewhat delayed arrival, with initiation
211 normally earlier in June (Gautam and Regmi, 2013; Immerzeel et al., 2014; Salerno et al.,
212 2015). A relative drying of the atmosphere at all sites and acceleration of the high-altitude
213 winds suggest termination around 1 October 2019, which is more consistent with the
214 climatological timing of cessation (Gautam and Regmi, 2013). The apparent brevity of the
215 monsoon is reflected in precipitation receipts, with the 558 mm recorded at Phortse since
216 installation (17 April 2019 to 31 October 2019) equivalent to around 90% of the climatological
217 monsoonal precipitation for this altitude in the Koshi River basin (Salerno et al., 2015)².

218 The delayed monsoon onset is recognisable in comparisons of our observations at the
219 South Col with those from the world's previous highest AWS operating there in 2008 (Moore
220 et al., 2012b), as our median June temperature was around 1.3°C lower, and the median wind

¹ The Base Camp station was offline from late May until mid-October due to a software bug (now corrected).

² Salerno et al. (2015) indicate mean annual precipitation (p) in the Koshi River basin can be modelled as a function of elevation, x , according to: $p = 21168e^{-0.0009x}$, and that around 90% of this falls during the monsoon.

221 speed was almost 3 m s^{-1} higher (Table 2). During July and August the temperatures and wind
222 speeds between years are in relatively close agreement, but Moore et al. (2012b) report much
223 stronger winds and lower air temperatures throughout September and October. Despite such
224 apparently subdued winds during the post monsoon period, our peak gust of 50.8 m s^{-1} exceeds
225 the all-time maximum wind speed by a factor of 1.12 for October estimated from the ERA-
226 Interim for the summit/South Col (45.3 m s^{-1} ; design specification section), a feat also achieved
227 by June's 39.8 m s^{-1} gust (1.16 times greater than the 34.3 m s^{-1} maximum for that month in
228 the ERA-Interim). These gust factors are well within the AWS design standard, but suggest
229 that the all-time maximum values plotted in Fig. 4 are a lower bound for the winds to anticipate
230 at the South Col. The Balcony AWS was evidently installed in a more sheltered location than
231 the Col, with generally lower winds despite the greater elevation (Fig. 4). Note that the slightly
232 reduced air pressure we recorded relative to 2008 in all months (Table 2) is consistent with the
233 marginally higher elevation of our AWS compared with the Italian installation site.

234 Another interesting feature of the early observations is the extraordinary receipts of
235 insolation at Phortse, Camp II and the South Col, where daily maximum values approach, and
236 occasionally exceed, the top-of-atmosphere incident flux (Fig. 4). Transmittance of solar
237 radiation increases with elevation (Bintanja, 1996), but some attenuation of insolation from
238 ozone, water vapor, and uniformly mixed gases should be anticipated (Pellicciotti et al., 2011).
239 Insolation exceeding the top-of-atmosphere potential has been reported before in the Himalaya,
240 and is thought to result from multiple reflections from nearby snow-covered surfaces and thin
241 clouds (de Kok et al., 2019). We suggest that further analysis of this phenomenon should be
242 considered, given the potential importance of shortwave radiation in driving high-altitude melt
243 and sublimation identified below.

244 **Sample Applications**

245 *Glacier-Climate Interactions*

246 The South Col and Camp II AWSs are instrumented to model the surface energy fluxes at
247 elevations rarely possible, offering the opportunity to improve regional simulations of glacier
248 mass balance in HMA. We explore the energetics at these locations using a model (detailed in
249 Appendix B) which computes all terms in the surface energy balance (SEB):

$$250 \quad 0 = Q_{SW} + Q_{LW} + Q_H + Q_L + Q_G + Q_M$$

251 Eq. 1

252 where Q_{SW} is the net shortwave heat flux, Q_{LW} is the net longwave heat flux, Q_H is the sensible
253 heat flux, Q_L is the latent heat flux, Q_G is the ground heat flux, and Q_M is the energy available
254 for melting. The SEB was modelled for a prescribed snow surface with constant albedo (0.8);
255 because the AWSs are located on bedrock proximate to the glacier (Figure 2), so we are unable
256 to monitor the evolving glacier surface directly.

257 Consistent with previous studies in the region (Kayastha et al., 1999; Litt et al., 2019),
258 and following from the high levels of insolation reported in the initial observations, the results
259 indicate that net shortwave radiation is the largest energy source for the surface at both sites
260 (Figure 5 and Table 3). Most of this energy is then dissipated by net longwave radiation, with
261 smaller amounts lost to the latent heat flux (sublimation) and consumed in melting. The SEB
262 modelling indeed indicates that the amount of potential meltwater generated at Camp II is non-
263 negligible, *despite* freezing air temperatures (Fig. 5; 77% of melt occurred when air
264 temperature was below 0°C). This conclusion was supported by streams of meltwater observed
265 in the vicinity of Camp II during May on the 2019 Everest Expedition, a month in which air
266 temperature did not rise above freezing for a single hour at the Camp II AWS. Importantly, this
267 behavior would not be captured by mass balance models that assume melting occurs only when
268 air temperatures exceed 0°C (Huss and Hock, 2015; Radić et al., 2014), indicating that such
269 methods may indeed be unsuitable for HMA (Litt et al., 2019). However, to what extent any
270 melt would contribute to runoff (rather than refreezing at some point before leaving the glacier)

271 remains to be determined. The anomalously warm borehole ice temperatures observed well
272 *above* the mean annual air temperature on the lower Khumbu Glacier by Miles et al. (2018) are
273 certainly consistent with significant latent heat release from refreezing of meltwater in the
274 Western Cwm.

275 The high insolation that could enable considerable melt to occur at Camp II may also
276 trigger melting at the South Col, with our simulation generating around 60 mm of meltwater
277 despite a peak daily mean air temperature of -10°C (on 30 July), and not a single hourly mean
278 air temperature above the melting point (maximum was -2.6°C on 7 July³). While such melt
279 totals cannot be confirmed, we do find evidence of the surface repeatedly reaching the melting
280 point during episodes of snow cover, when there is also generally good agreement between
281 observed and modelled surface temperatures, despite the simplicity of our idealized snow
282 surface (Appendix C). These SEB results therefore indicate snowmelt is possible right up to
283 the altitude of the South Col, meaning melting may be not be uncommon up to the very tops of
284 all but a handful of the highest mountains in the Himalaya (only 14 peaks on Earth are above
285 8,000 m.a.s.l). For the South Col itself, we also expect that substantially more melt occurs than
286 indicated for the idealized snow surface, as glacier ice is exposed at the South Col. Re-running
287 the SEB model for such a plausible ice surface suggests melt totals of over 2 m are possible
288 (Appendix B). The substantial increase is consistent with a very strong sensitivity to albedo,
289 which follows from the high levels of insolation.

290 The SEB analysis raises the question as to whether melt may even occur at the summit
291 of Everest. We provide a first order assessment of this by conservatively⁴ extrapolating
292 meteorological variables to 8,850 m.a.s.l and rerunning the SEB model for the same prescribed
293 snow surface. Uncertainties in the extrapolation are considerable (Appendix D), but we *cannot*

³ We caution that the highest temperatures may be prone to positive bias if observed during strong solar heating and low wind speeds. This value occurred under winds of only 0.2 m s^{-1} and insolation of $1,161\text{ W m}^{-2}$.

⁴ Summit temperatures were estimated with a method designed to be robust to solar heating of temperature sensors in the AWS network (Appendix D).

294 rule out that limited melting during the monsoon may be occurring at the summit (Fig. 6). We
295 find four days on which the simulated surface temperature reached the melting point under
296 light winds and high relative humidity (generally over 80%). Under such conditions turbulent
297 and longwave dissipation of the intense shortwave is suppressed, permitting modelled melt
298 with air temperatures below -12°C .

299 Although melting at the highest point on Earth may have strong symbolic significance,
300 sublimation seems to be a far greater means of mass loss at extreme altitude on Everest, with
301 over 100 mm simulated for the summit and South Col (Fig. 5 and 6). The higher totals at these
302 altitudes compared with that at Camp II (less than 50 mm) reflect the increased winds higher
303 on the mountain that enable latent heat transfer to more efficiently dissipate the net solar
304 radiation, which also amplifies with altitude (Table 3). The amount of mass potentially lost by
305 sublimation on the upper slopes of Everest, coupled with the presence of permanent snow cover
306 over much of this terrain, raises the interesting prospect that snowfall at such altitudes in the
307 Himalaya may be more substantial than previously thought. For example, the modelled
308 sublimation of 128 mm at the South Col (in five months) is almost eight times greater than the
309 predicted *annual* precipitation at such altitude (Salerno et al., 2015). Windblown snow from
310 lower elevations may account for much of the discrepancy, but the winds are also known to
311 deflate the snow on Everest, sometimes to spectacular effect (Moore, 2004). Future work is
312 clearly needed to rule out the possibility of a much more vigorous hydrological cycle at these
313 extreme elevations. .

314 ***Improved Everest Weather Forecasts***

315 Ascending to the summit of Everest requires the relatively light winds characteristic of high-
316 pressure conditions, with climbers otherwise at much greater risk from cold injury and death
317 (Firth et al., 2008; Moore and Semple, 2011). The performance of forecasts made in support of
318 climbing expeditions is largely unknown due to the absence of in-situ observations for

319 evaluation. We demonstrate another sample application of the new AWS data here by
 320 addressing this gap to provide the first comparison of numerical weather forecasts against
 321 actual observations from high on Everest.

322 During the 2019 Everest Expedition, our AWS installation team used operational
 323 deterministic forecasts from the 0.25° version of the Global Forecast System (GFS) run by the
 324 United States National Weather Service, and from the 0.1° HRES model run by the ECMWF.
 325 We assess the performance of these models here over the concurrent period that the AWSs
 326 have been operating, and that we have been archiving the forecasts (6 June to 31 October 2019).
 327 The forecasts are assessed for wind speed (which is often the limiting factor deciding when to
 328 climb) using data interpolated from pressure levels (for the GFS) and from model levels (for
 329 HRES) to the locations of the South Col AWS, the windiest of the locations monitored (see
 330 initial observations). Forecast skill is quantified for each forecast lead time (t) using the mean
 331 absolute error (mae):

$$332 \quad mae(t) = \frac{1}{n} \sum_{i=1}^{i=n} |o_i - y_i|$$

333 Eq. 2.

334 where o denotes the hourly-mean wind speeds observed at the South Col AWS, and y is the
 335 mean wind speed from the respective forecasts. Skill scores (SS) are used as a basis to compare
 336 forecasts (Wilks, 2011):

$$337 \quad SS(t) = 1 - \frac{mae}{mae_{ref}}$$

338 Eq. 3

339 where we begin by calculating mae_{ref} from a simple forecast of persistence for different lead
 340 times:

$$341 \quad mae_{ref}(t) = \frac{1}{n-t} \sum_{i=t+1}^{i=n} |o_{i-t} - o_i|$$

342

Eq. 4

343 With $SS > 1$ the results indicate that, except for 24-hour HRES, both models are an
 344 improvement on the persistence forecast. They also show without exception that mae is
 345 smallest for the GFS at all lead times (Fig. 7). However, correlations between the forecast and
 346 observed wind speeds indicate strong covariation, enabling application of Model Output
 347 Statistics (MOS) (Carter et al., 1989) through linear regression to improve the forecasts. We
 348 pursue this here using separate coefficients for each lead time, with the MOS prediction given
 349 by:

350

$$X_{MOS}(t) = \alpha_t + \beta_t X_t$$

351

Eq. 5

352 in which X_t is the raw wind speed forecast. The updated SS values (now defined with mae_{ref}
 353 calculated on the uncorrected forecasts) indicate that applying MOS improves both models, but
 354 most notably HRES, which now outperforms the GFS at all lead times considered (Fig. 7).
 355 To explore the skill of these MOS forecasts in more detail, we focus on hourly mean winds for
 356 a forecast lead time of 48-hours. This time horizon is critical for planning the final and most
 357 dangerous climbing stage because mountaineers attempt the summit approximately this long
 358 after deciding to leave Camp II on Everest's main southern climbing route. We also highlight
 359 in Figure 7 the performance in the pre-monsoon period of June (see initial observations for
 360 timing of the monsoon) because this is the season when most climbing takes place (Hawley
 361 and Salisbury, 2007). Both models capture the timing of enhanced winds, which peaked in
 362 early June when wind gusts were of a similar strength to those estimated for the infamous and
 363 deadly 1996 storm (Fig. 4; Moore and Semple, 2006). HRES MOS also captures the magnitude
 364 of these winds well, but GFS MOS underestimates their intensity (by ~30%).

365 The ability of both models to correctly forecast rapid acceleration in the winds is
 366 encouraging, particularly given the somewhat modest ability noted of reanalysis data to capture

367 the passage of extremes (Moore and Semple, 2004). This improvement may be because the
368 GFS and HRES have relatively high spatial resolutions compared with reanalyses, or because
369 the enhanced winds in June 2019 reflected synoptic-scale strengthening, instead of localised
370 convection as in earlier case studies (Moore and Semple, 2006, 2004). More detailed analysis
371 during the pre-monsoon period is required to resolve this, which we hope will be facilitated by
372 continued data collection from the high-altitude AWSs through at least spring 2020. In any
373 case, this preliminary assessment of forecast performance suggests considerable scope for
374 enhancing the safety of those trying to summit Everest. As the now owner of the AWSs, the
375 Nepalese Department of Hydrology and Meteorology will build on this potential (and the near
376 real-time data feed from the AWSs) to generate more accurate, publicly available forecasts and
377 warnings for mountaineers, at altitudes where weather predictability has been limited. This,
378 along with additional avenues for future research, are discussed below.

379 **Synthesis and Outlook**

380 We have described the motivation, design, and installation of the highest weather station
381 network on Earth, whose measurements hold the potential to improve understanding of
382 Everest's weather and ongoing climate change across the full altitudinal range of glaciers in
383 HMA. This potential of the network has been demonstrated in sample applications, providing
384 initial insights into potential surface energy fluxes high in the accumulation area of the Khumbu
385 Glacier and the first assessment of weather forecasts for the summit slopes of Everest. As the
386 AWSs enter their first winter, we await the seasonal formation of the jet stream winds (Galvin,
387 2007). We anticipate that AWS observations during jet episodes will enable improved
388 understanding of dangerous weather events on Everest (Firth et al., 2008; Moore and Semple,
389 2006), aeolian transport of pollutants (Bonasoni et al., 2008) and, longer-term, the response of
390 this globally-significant wind to climate warming. Such insights may be generated using multi-
391 decadal climate reconstructions to extend short records from the AWSs (Wilby et al., 2014),

392 but longevity of the network is clearly preferable to track emerging trends. Collaborating with
393 the Everest climbing community to maintain the high-altitude AWSs is, therefore, a high
394 priority. At the time of writing we are working closely with Nepalese research and climbing
395 partners to plan the first maintenance visit targeted for 2020. We are also working with
396 colleagues from China to consolidate the records from the AWS network reported here with
397 observations from the north side of Everest, collected by an AWS deployed at 6,475 m.a.s.l by
398 a Chinese team in spring 2019, whose field efforts ran concurrently to our own.

399 In the near term, the data collected so far already offer rich opportunities to refine the
400 mountain weather forecasting and melt modelling applications introduced here. For example,
401 there is scope for the network to serve as a high-profile testing ground for developing machine
402 learning techniques to forecast hazardous weather in complex terrain (Ii et al., 2015), and for
403 enabling the development of transferrable empirical models that can capture mass losses high
404 in the accumulation zones of glaciers in HMA (Litt et al., 2019). We also note that, with a
405 recent resurgence in attempts to climb Everest in winter without supplementary oxygen
406 (Pokhrel, 2019), there is a strong incentive to forecast oxygen availability (through its
407 relationship with air pressure) on Everest's upper slopes. Summit conditions are, on average,
408 very close to the tolerance limit of hypoxia, and the relatively large pressure fluctuations in
409 winter may push conditions dangerously close to (or beyond) this threshold (Moore and
410 Semple, 2009; Moore et al., 2012b; West et al., 1983).

411 Further work may also continue exploring processes of mass loss on Everest's summit.
412 Our analysis has raised the prospect that the summit is *at least close to* melting during the
413 monsoon season. Although this cannot be confirmed until direct AWS measurements of surface
414 temperature reach the summit itself, future refinements to modelling the SEB may more tightly
415 constrain its probability of occurrence, and how sensitive this is to climate warming. Melting
416 at the summit of Everest -- already observed or still yet to occur -- could mark the crossing of

417 a symbolic threshold in demonstrating the impacts of climate change on our planet's most
418 extreme environments.

419 **Data and Code Availability**

420 The raw, hourly AWS data used in this study are available for download here:

421 <https://www.nationalgeographic.org/projects/perpetual-planet/everest/weather-data/>

422 The computer code used to model the surface energy balance is available here:

423 https://github.com/climatom/Everest_BAMS.git

424 **Acknowledgements**

425 This research was conducted in partnership with National Geographic Society, Rolex, and
426 Tribhuvan University, with approval from all relevant agencies of the Government of Nepal.

427 We acknowledge Conrad Anker and Peter Athans as inspirational mountaineers who prepared
428 the 2019 Everest expedition team and kept them safe. We also wish to thank the communities

429 of the Khumbu Region, Xtreme Climbers Treks and Expedition P. Ltd, and Jiban Ghimire and
430 Shangri-La Nepal Trek Pvt. Ltd, and we further recognise the extraordinary efforts of our entire

431 Sherpa climbing team, whose physical and mental prowess at altitude made installation of the
432 AWSs possible. The core AWS-installation team members were: Panuru Sherpa (Sirdar), Phu

433 Tashi Sherpa, Pemba Sherpa, Urken Lendu Sherpa, Ila Nuru Sherpa, Fura Chetten
434 Sherpa, Lakpa Gyaljen Sherpa, Pasang Sona Sherpa, Pasang Kami Sherpa, Nima Rita Sherpa,

435 Tenzing Gyanjen Sherpa, and Nawang Phinjo Sherpa. Dawa Yangzum Sherpa, Amrit Ale,
436 Mark Fisher, Dirk Collins, and Eric Daft are also thanked for helping to ensure a successful

437 and safe climb conducted with good humor. Heather Guy is thanked for forecasting support,
438 Mike Hughes and Dana Greene for AWS design considerations, and the team of engineers at

439 Campbell Scientific, Inc (Mike Hansen, Jared Campbell, Steve Gunderson, and Gary Roberts)
440 are acknowledged for designing the AWSs. Gian Pietro Verza is thanked for his help planning

441 installation, Patrick Wagnon and Keith Garrett for helpful advice, and the European Centre for
442 Medium Range Weather Forecasts is gratefully acknowledged for providing access to its

443 forecasts. We also thank G.W.K. Moore, one anonymous reviewer, and Fae Jencks at National
444 Geographic for their help in improving the communication of our study.

445 **Appendices**

446 **APPENDIX A**

447 **Database of Existing Automatic Weather Stations**

448 In the main text we present the current distribution of automatic weather stations (AWSs)
449 worldwide. To assemble this, we downloaded the positions of all the active AWSs in the
450 Integrated Surface Database (Smith et al., 2011), and then supplemented these with all
451 information on high-altitude AWSs presently known to the authors. The compiled station list
452 is available for download here: <https://tinyurl.com/y2lgx33o>.

453 **APPENDIX B**

454 **Modelling the Surface Energy Balance**

455 Here we present the methods used to compute the surface energy balance (SEB) for a
456 hypothetical snow surface at the elevations of the Camp II and South Col AWSs. We start from
457 recalling that the SEB can be written:

$$458 \quad 0 = Q_{SW} + Q_{LW} + Q_H + Q_L + Q_G + Q_M$$

459 Eq. A1

460 in which Q_{SW} is the net shortwave heat flux, Q_{LW} is the net longwave heat flux, Q_H is the
461 sensible heat flux, Q_L is the latent heat flux, Q_G is the ground heat flux, and Q_M is the energy
462 available for melting. All fluxes are defined as positive when directed toward the surface.

463 We computed Q_{SW} from:

$$464 \quad Q_{SW} = S_i(1 - \alpha)$$

465 Eq. A2

466 where S_i is the incident flux of solar radiation measured at the AWS, and α is the albedo. We
467 set α to be 0.80 -- a value on the high side for old snow (Oke, 2009), but close to that measured

468 with a handheld spectrometer by the 2019 Everest field team over an (old) snow surface at
 469 Camp II (0.83).

470 Q_{LW} is the difference between the incident longwave flux recorded by the AWS (L_i) and that
 471 emitted by the snow surface at temperature, T_s , which has an emissivity of ε :

$$472 \quad Q_{LW} = L_i - \sigma \varepsilon T_s^4$$

473 Eq. A3

474 in which σ is the Stefan Boltzmann constant. In our model, we use $\varepsilon = 0.98$ (Tonboe et al.,
 475 2011).

476 The turbulent heat fluxes (Q_H and Q_L) were computed using the bulk aerodynamic
 477 method (Hock, 2005):

$$478 \quad Q_H = C_H \rho c_p V (T_a - T_s)$$

479 Eq. A4

$$480 \quad Q_L = C_L \rho L_v V (q_a - q_s)$$

481 Eq. A5

482 in which C_H and C_L are the exchange coefficients for heat and moisture, respectively; ρ is air
 483 density; c_p is the specific heat capacity of the air ($1005 \text{ J kg}^{-1} \text{ K}^{-1}$); and L_v is the latent heat of
 484 vaporization (2501 kJ kg^{-1}); and V is the wind speed. T and q in Eqs. A4 and A5 denote the air
 485 temperature and specific humidity recorded at the AWS (subscript a) and are modelled for the
 486 surface (subscript s). The exchange coefficients were calculated according to:

$$487 \quad C_H = \frac{k^2}{[\ln\left(\frac{z}{z_0}\right) - \psi_M\left(\frac{z}{L}\right)] [\ln\left(\frac{z}{z_{oT}}\right) - \psi_H(z/L)]}$$

488 Eq. A6

$$489 \quad C_L = \frac{k^2}{[\ln\left(\frac{z}{z_0}\right) - \psi_M\left(\frac{z}{L}\right)] [\ln\left(\frac{z}{z_{oE}}\right) - \psi_E(z/L)]}$$

490 Eq. A7

491 where $k = 0.4$ is the von Kármán constant, L is the Monin-Obukhov length, z is the
 492 measurement height (m), z_0 is the roughness length for momentum, z_{oT} is the roughness length
 493 for heat, and z_{oE} is the roughness length for humidity. We prescribe z_0 to be 0.0027 m and set
 494 z_{oT} and z_{oE} to be one order of magnitude smaller. This value for z_0 is equal to the mean of
 495 those reported for snow cover on low-latitude glaciers by Brock et al. (2006), and the scaling
 496 to z_{oT} and z_{oE} is consistent with that found by Stigter et al. (2018) using eddy-covariance
 497 measurements at over 5,000 m.a.s.l on Yala Glacier (also in Nepal). The roughness lengths
 498 may, however, not be appropriate for the high-altitude snow-covered glaciers in the Himalaya.
 499 We therefore tested the sensitivity of the results by rerunning the SEB simulations with z_0 set
 500 to the 5th (0.0009 m) and 95th (0.0057 m) percentiles of the roughness lengths reported by Brock
 501 et al. (2006) for low-latitude snow covered glaciers. All cumulative melt and sublimation totals
 502 were then presented as an envelope bounded by results from simulations run with these upper
 503 and lower roughness lengths. The stability functions ψ for momentum, heat, and moisture
 504 (subscripts M , H and E , respectively) were applied to extend the bulk aerodynamic approach
 505 to non-neutral boundary layers. For unstable cases, ψ was parameterized using the expressions
 506 of Dyer (1974); those from Holtslag and De Bruin (1988) were used for stable conditions.
 507 L requires Q_H , which introduces circularity to the SEB computation. We therefore adopted an
 508 iterative technique following Munro (1990), whereby Q_H was initialized assuming a neutral
 509 boundary layer (and the ψ_M terms are omitted from Eqs. A6 and A6); L , ψ , and Q_H were then
 510 updated with each iteration until the change in Q_H was smaller than 1%.

511 Evaluation of the turbulent and longwave heat fluxes requires knowledge of T_s . We
 512 modelled this for the hypothetical snow surface by initializing $T_s = T_A$, and then evolving T_s .
 513 according to the scheme proposed by Wheler and Flowers (2011):

$$514 \quad \Delta T_s = - \frac{Q_g}{\rho_s c_s h} \Delta t$$

515 Eq. A8

516 where c_s and ρ_s are, respectively, the specific heat capacity of ice (2097 J kg⁻¹ K⁻¹) and the
517 density in a surface layer of depth h . We used $\rho_s = 530$ kg m⁻³ consistent with the mean density
518 measured in an 80-cm snow pit at Camp II during the 2019 Everest Expedition; h was set to
519 0.1 m (MacDougall and Flowers, 2010). To prevent unrealistically low surface temperature,
520 we follow Wheler and Flowers (2011), limiting T_s to a lower threshold of T_c (-40°C here), and
521 tracking additional heat losses by defining cold content (C) in a passive, secondary subsurface
522 layer:

$$523 \quad C = \frac{T_s - T_c}{\Delta t} \rho_s c_s c_s h$$

524 Eq. A9

525 The ground heat flux (Q_g) (which determines the evolution of T_s) was computed from:

$$526 \quad -Q_g = (Q_{SW} + Q_{LW} + Q_H + Q_L)$$

527 Eq. A10

528 unless calculated T_s would exceed 0°C and the cold content from the passive, subsurface layer
529 had been eliminated (i.e. $C = 0$), in which case $Q_g = 0$ and melt energy (Q_M) was computed
530 as:

$$531 \quad Q_M = \max\left(\frac{(T_s \rho_s c_s h - C)}{\Delta t}, 0\right)$$

532 Eq. A11

533 where T_s is in °C. Note that after Eq. A11 is applied, T_s is reset to 0°C and C is reduced to
534 $\max(C - T_s \rho_s c_s h, 0)$. We divided Q_M by the latent heat of fusion (334 kJ kg⁻¹) to convert melt
535 energy to millimeters of water equivalent. Sublimation was derived from the latent heat flux.

536 To ensure numerical stability, we calculated the SEB at a time-step of 120 s after having
537 interpolated hourly AWS data to this temporal resolution. We also performed some pre-
538 processing of the radiation measurements. First, we used calculated top-of-atmosphere

539 insolation to set all nighttime values of S_i and S_o to zero. Second, we identified periods when
540 S_o exceeded S_i (~6% of observations at the South Col, ~1% at Camp II). We interpret this as
541 resulting from snow covering the upward-facing pyranometer, so these S_i values were replaced
542 with $S_o \times 1/\min(0.9, \alpha_{acc})$, where α_{acc} is the “accumulated albedo”, defined as the mean
543 24-hour albedo centered on the time-step of interest (Azam et al., 2014; van den Broeke et al.,
544 2004). In the third correction step, we replaced the measured incident longwave radiation
545 during these periods of suspected snow-cover with estimates derived from the parameterization
546 of de Kok et al. (2019), using coefficients optimized for the locations of the AWSs.

547 To investigate the sensitivity of the energy balance simulations to surface type, we
548 repeated the modelling for a prescribed glacier ice surface, with an albedo of 0.4 (measured
549 over clean ice at Base Camp with a Hukseflux NR01 pyranometer), and a near-surface density
550 of 910 kg m^{-3} (Fig. A1). This experiment yields insight into actual melt rates at the South Col,
551 where there is abundant exposed ice (Fig. A2),

552 **APPENDIX C**

553 **Validating Melt Occurrences at the South Col**

554 We attempted to verify our conclusion that melting is possible at the South Col using the
555 outgoing longwave flux measured at the AWS there. We made use of the fact that emitted
556 longwave radiation (L_o) can be modelled with $\sigma \epsilon T_s^4$ (see Eq. A3), and that when the surface
557 is at the melting point $T_s=273.15$ so $L_o= 309.3 \text{ W m}^{-2}$ for $\epsilon = 0.98$. However, the AWS is
558 situated over bedrock, so to detect melt events we limited our assessment using the measured
559 shortwave heat fluxes at the South Col to identify periods of snow with an albedo similar (\pm
560 0.1) to the 0.8 prescribed in the SEB model. For this comparison, we also set z_o to 0.0002 m
561 (maintaining z_{oT} and z_{oE} to be one order of magnitude smaller), which is representative of
562 fresh snow in the low latitudes (Brock et al., 2006). Examining the South Col measurements in
563 this way suggests the following: (1) snowmelt can indeed occur at the South Col, and (2) the

564 SEB model realistically captures its timing, with almost 70% of the melt days identified by the
 565 SEB model also detected by the observations during the period of snow cover (Fig. A3). As
 566 further support for the realism of the SEB modelling (and the conclusion that melt is possible),
 567 we note the high correlation ($r = 0.93$) and limited bias (particularly at the higher end of the
 568 range), in daily mean modelled and observed surface temperatures at the South Col during
 569 periods of snow cover (Figure. A4).

570 APPENDIX D

571 Estimating the Summit Weather

572 To assess possible mass losses through ablation and melt at the summit, we estimated the
 573 summit weather using data from the lower AWSs. For relative humidity and transmissivity (τ :
 574 the ratio of received to top-of-atmosphere insolation), summit values (Y_t) were computed at
 575 hour t from

$$576 \quad Y_t = \alpha_t + \beta_t z$$

577 Eq. A12

578 where α and β are, respectively, the intercept and slope coefficients obtained from regressing
 579 the hourly mean meteorological quantity (Y_t) across the AWSs against their elevations (z).
 580 Note that, before applying the regression for τ , we first computed running values, defined as
 581 ratio of the 24-hour sums of received, to top-of-atmosphere, insolation. We then multiplied the
 582 regression-estimated τ for the summit by the hourly top-of-atmosphere flux to estimate summit
 583 insolation.

584 The summit temperature was estimated with a similar linear regression technique:

$$585 \quad Y_t = Y_{t,z} + \beta_t \Delta z$$

586 Eq. A13

587 This time, $Y_{t,z}$ is the air temperature at AWS with the highest concurrent mean hourly wind
 588 speed, and β_t is the slope of the regression line relating elevation to the 24-hour running-mean

589 air temperature at each site; Δz is the difference in elevation between the summit and the AWS
 590 with the highest mean hourly wind speed. By extrapolating air temperatures from the windiest
 591 AWS in this way, we aim to minimize positive bias in our summit air temperature estimate
 592 resulting from solar heating of temperature sensors during periods of high insolation and light
 593 winds.

594 The summit wind was parameterized assuming that, because the summit *cannot* be
 595 sheltered by the surrounding topography, its hourly mean speed (V_t) can be estimated as the
 596 fastest of the winds observed at either the South Col or the Balcony (the most exposed AWSs),
 597 multiplied by a scalar to account for the reduced air density at the summit (and hence greater
 598 velocity for the same driving pressure gradient (Stull, 2015)):

$$599 \quad V_t = \max(V_{t,South\ Col}, V_{t,Balcony}) \frac{\rho_{t,x}}{\rho_{t,summit}}$$

600 Eq. A14

601 where $\rho_{t,x}$ is the air density at either the Balcony or the South Col, whichever has the higher
 602 hourly mean wind speed. Note that summit air density was calculated using the ideal gas law
 603 and summit air pressure, which was estimated using the hypsometric equation and the air
 604 pressure measured at Balcony:

$$605 \quad P_t = P_{t,Balcony} \exp\left(\frac{8430 - 8850}{\frac{\mathcal{R}_d}{|g|} \bar{T}_t}\right)$$

606 Eq. A15

607 Where $\frac{\mathcal{R}_d}{|g|}$ is the gas constant for dry air divided by the magnitude of gravitational acceleration,
 608 and \bar{T}_t is the mean virtual air temperature in the atmospheric layer between the Balcony and
 609 the summit. We approximated this as the arithmetic mean of the (dry bulb) air temperature at
 610 the Balcony and (estimated) at the summit.

611 Finally, we parameterized incident longwave radiation using the method of de Kok et
612 al. (2019), with coefficients optimized for the South Col (the highest AWS equipped with a
613 longwave radiation sensor), and values of relative humidity and air temperature estimated for
614 the summit.

615 Uncertainties for the inferred summit weather are shown in Table A1. They were
616 estimated for temperature and relative humidity as 1.96 times the prediction standard deviation
617 from the hourly elevation-based regressions (Wilks, 2011); for insolation the same procedure
618 was used to determine uncertainty in τ , before multiplying this by the concurrent top-of-
619 atmosphere insolation. We restricted this assessment of insolation to daylight hours to avoid a
620 low bias. Note that these uncertainties computed through regression are obtained for each hour
621 and are summarized in Table A1 with the median.

622 Because longwave radiation was computed for the summit using empirical coefficients
623 optimized for the South Col, forced with relative humidity and temperature estimated for the
624 summit, there is opportunity for compounding errors. We neglect this complexity here and
625 report a *lower bound* on the uncertainty, calculated as the 95th percentile in absolute differences
626 between observed and modelled incident longwave radiation (using the method of de Kok et
627 al. (2019) at the South Col.

628 Given the different exposures of the AWSs, it is challenging to test our wind-speed
629 extrapolation between locations. We therefore do not attempt to quantify errors in summit wind
630 speed, but caution that this source of uncertainty is likely to be large.

631 **References Cited**

- 632
633 Abish, B., Joseph, P.V., Johannessen, Ola.M., 2015. Climate change in the subtropical
634 jetstream during 1950–2009. *Adv. Atmos. Sci.* 32, 140–148.
635 <https://doi.org/10.1007/s00376-014-4156-6>
636 Ágústsson, H., Ólafsson, H., 2004. Mean gust factors in complex terrain. *Meteorologische*
637 *Zeitschrift* 13, 149–155.
638 Azam, M.F., Wagnon, P., Vincent, C., Ramanathan, A.L., Favier, V., Mandal, A., Pottakkal,
639 J.G., 2014. Processes governing the mass balance of Chhota Shigri Glacier (western

- 640 Himalaya, India) assessed by point-scale surface energy balance measurements. *The*
641 *Cryosphere* 8, 2195–2217. <https://doi.org/10.5194/tc-8-2195-2014>
- 642 Bertolani, L., Bollasina, M., Tartari, G., 2000. Recent biennial variability of meteorological
643 features in the eastern Highland Himalayas. *Geophysical Research Letters* 27, 2185–
644 2188. <https://doi.org/10.1029/1999GL011198>
- 645 Bintanja, R., 1996. The Parameterization of Shortwave and Longwave Radiative Fluxes for
646 Use in Zonally Averaged Climate Models. *J. Climate* 9, 439–454.
647 [https://doi.org/10.1175/1520-0442\(1996\)009<0439:TPOSAL>2.0.CO;2](https://doi.org/10.1175/1520-0442(1996)009<0439:TPOSAL>2.0.CO;2)
- 648 Bonasoni, P., Laj, P., Angelini, F., Arduini, J., Bonafè, U., Calzolari, F., Cristofanelli, P.,
649 Decesari, S., Facchini, M.C., Fuzzi, S., Gobbi, G.P., Maione, M., Marinoni, A.,
650 Petzold, A., Roccato, F., Roger, J.C., Sellegri, K., Sprenger, M., Venzac, H., Verza,
651 G.P., Villani, P., Vuillermoz, E., 2008. The ABC-Pyramid Atmospheric Research
652 Observatory in Himalaya for aerosol, ozone and halocarbon measurements. *Science of*
653 *The Total Environment, Research at Jungfrauoch - Contributions to the International*
654 *conference in celebration of the 75th anniversary of the High Altitude Research*
655 *Station Jungfrauoch at Interlaken, Switzerland (11-13 September, 2006)* 391, 252–
656 261. <https://doi.org/10.1016/j.scitotenv.2007.10.024>
- 657 Bradley, R.S., Keimig, F.T., Diaz, H.F., Hardy, D.R., 2009. Recent changes in freezing level
658 heights in the Tropics with implications for the deglaciation of high mountain
659 regions. *Geophysical Research Letters* 36. <https://doi.org/10.1029/2009GL037712>
- 660 Brock, B.W., Willis, I.C., Sharp, M.J., 2006. Measurement and parameterization of
661 aerodynamic roughness length variations at Haut Glacier d’Arolla, Switzerland.
662 *Journal of Glaciology* 52, 281–297. <https://doi.org/10.3189/172756506781828746>
- 663 Carrasco, J.F., Casassa, G., Quintana, J., 2005. Changes of the 0°C isotherm and the
664 equilibrium line altitude in central Chile during the last quarter of the 20th century /
665 Changements de l’isotherme 0°C et de la ligne d’équilibre des neiges dans le Chili
666 central durant le dernier quart du 20ème siècle. *Hydrological Sciences Journal* 50,
667 null-948. <https://doi.org/10.1623/hysj.2005.50.6.933>
- 668 Carter, G.M., Dallavalle, J.P., Glahn, H.R., 1989. Statistical Forecasts Based on the National
669 Meteorological Center’s Numerical Weather Prediction System. *Wea. Forecasting* 4,
670 401–412. [https://doi.org/10.1175/1520-0434\(1989\)004<0401:SFBOTN>2.0.CO;2](https://doi.org/10.1175/1520-0434(1989)004<0401:SFBOTN>2.0.CO;2)
- 671 de Kok, R.J., Steiner, J.F., Litt, M., Wagnon, P., Koch, I., Azam, M.F., Immerzeel, W.W.,
672 2019. Measurements, models and drivers of incoming longwave radiation in the
673 Himalaya. *International Journal of Climatology* 0. <https://doi.org/10.1002/joc.6249>
- 674 Dee, D.P., Uppala, S.M., Simmons, A.J., Berrisford, P., Poli, P., Kobayashi, S., Andrae, U.,
675 Balmaseda, M.A., Balsamo, G., Bauer, P., Bechtold, P., Beljaars, A.C.M., van de
676 Berg, L., Bidlot, J., Bormann, N., Delsol, C., Dragani, R., Fuentes, M., Geer, A.J.,
677 Haimberger, L., Healy, S.B., Hersbach, H., Hólm, E.V., Isaksen, L., Kållberg, P.,
678 Köhler, M., Matricardi, M., McNally, A.P., Monge-Sanz, B.M., Morcrette, J.-J., Park,
679 B.-K., Peubey, C., de Rosnay, P., Tavolato, C., Thépaut, J.-N., Vitart, F., 2011. The
680 ERA-Interim reanalysis: configuration and performance of the data assimilation
681 system. *Q.J.R. Meteorol. Soc.* 137, 553–597. <https://doi.org/10.1002/qj.828>
- 682 Dyer, A.J., 1974. A review of flux-profile relationships. *Boundary-Layer Meteorol* 7, 363–
683 372. <https://doi.org/10.1007/BF00240838>
- 684 Firth, P.G., Zheng, H., Windsor, J.S., Sutherland, A.I., Imray, C.H., Moore, G.W.K., Semple,
685 J.L., Roach, R.C., Salisbury, R.A., 2008. Mortality on Mount Everest, 1921-2006:
686 descriptive study. *BMJ* 337, a2654. <https://doi.org/10.1136/bmj.a2654>
- 687 Galvin, J.F.P., 2007. The weather and climate of the tropics Part 2 –The subtropical jet
688 streams. *Weather* 62, 295–299. <https://doi.org/10.1002/wea.65>

- 689 Gautam, D., Regmi, S., 2013. Recent Trends in the Onset and Withdrawal of Summer
690 Monsoon over Nepal. *ECOPERSIA* 1, 353–367.
- 691 Hawley, E., Salisbury, R., 2007. The Himalayan database: The expedition archives of
692 Elizabeth Hawley.
- 693 Hock, R., 2005. Glacier melt: a review of processes and their modelling. *Progress in Physical
694 Geography: Earth and Environment* 29, 362–391.
695 <https://doi.org/10.1191/0309133305pp453ra>
- 696 Holtslag, A. a. M., De Bruin, H. a. R., 1988. Applied Modeling of the Nighttime Surface
697 Energy Balance over Land. *J. Appl. Meteor.* 27, 689–704.
698 [https://doi.org/10.1175/1520-0450\(1988\)027<0689:AMOTNS>2.0.CO;2](https://doi.org/10.1175/1520-0450(1988)027<0689:AMOTNS>2.0.CO;2)
- 699 Huss, M., Hock, R., 2015. A new model for global glacier change and sea-level rise. *Front.
700 Earth Sci.* 3. <https://doi.org/10.3389/feart.2015.00054>
- 701 Ii, D.J.G., McGovern, A., Brotzge, J., Coniglio, M., Jr, J.C., Xue, M., 2015. Day-Ahead Hail
702 Prediction Integrating Machine Learning with Storm-Scale Numerical Weather
703 Models, in: Twenty-Seventh IAAI Conference. Presented at the Twenty-Seventh
704 IAAI Conference.
- 705 Immerzeel, W.W., Beek, L.P.H. van, Bierkens, M.F.P., 2010. Climate Change Will Affect
706 the Asian Water Towers. *Science* 328, 1382–1385.
707 <https://doi.org/10.1126/science.1183188>
- 708 Immerzeel, W.W., Lutz, A.F., Andrade, M., Bahl, A., Biemans, H., Bolch, T., Hyde, S.,
709 Brumby, S., Davies, B.J., Elmore, A.C., Emmer, A., Feng, M., Fernández, A.,
710 Haritashya, U., Kargel, J.S., Koppes, M., Kraaijenbrink, P.D.A., Kulkarni, A.V.,
711 Mayewski, P., Nepal, S., Pacheco, P., Painter, T.H., Pellicciotti, F., Rajaram, H.,
712 Rupper, S., Sinisalo, A., Shrestha, A.B., Viviroli, D., Wada, Y., Xiao, C., Yao, T.,
713 Baillie, J.E.M., 2019. Importance and vulnerability of the world’s water towers.
714 *Nature* 1–1. <https://doi.org/10.1038/s41586-019-1822-y>
- 715 Immerzeel, W.W., Petersen, L., Ragetti, S., Pellicciotti, F., 2014. The importance of
716 observed gradients of air temperature and precipitation for modeling runoff from a
717 glacierized watershed in the Nepalese Himalayas. *Water Resources Research* 50,
718 2212–2226. <https://doi.org/10.1002/2013WR014506>
- 719 Kattel, D.B., Yao, T., Yang, K., Tian, L., Yang, G., Joswiak, D., 2013. Temperature lapse
720 rate in complex mountain terrain on the southern slope of the central Himalayas.
721 *Theor Appl Climatol* 113, 671–682. <https://doi.org/10.1007/s00704-012-0816-6>
- 722 Kayastha, R.B., Ohata, T., Ageta, Y., 1999. Application of a mass-balance model to a
723 Himalayan glacier. *Journal of Glaciology* 45, 559–567.
724 <https://doi.org/10.3189/S002214300000143X>
- 725 Krishnan, R., Shrestha, Arun B., Ren, G., Rajbhandari, R., Saeed, S., Sanjay, J., Syed, Md.A.,
726 Vellore, R., Xu, Y., You, Q., Ren, Y., 2019. Unravelling Climate Change in the
727 Hindu Kush Himalaya: Rapid Warming in the Mountains and Increasing Extremes,
728 in: Wester, P., Mishra, A., Mukherji, A., Shrestha, Arun Bhakta (Eds.), *The Hindu
729 Kush Himalaya Assessment: Mountains, Climate Change, Sustainability and People.*
730 Springer International Publishing, Cham, pp. 57–97. https://doi.org/10.1007/978-3-319-92288-1_3
- 731
- 732 Lau, M.B., 1998. GEOPAK: Monitoring climbers and climate on Mount Everest (M.S.).
733 Mass. Inst. of Technology, Cambridge.
- 734 Litt, M., Shea, J., Wagon, P., Steiner, J., Koch, I., Stigter, E., Immerzeel, W., 2019. Glacier
735 ablation and temperature indexed melt models in the Nepalese Himalaya. *Scientific
736 Reports* 9, 5264. <https://doi.org/10.1038/s41598-019-41657-5>
- 737 Locci, F., Melis, M.T., Dessì, F., Stocchi, P., Akinde, M.O., Bønes, V., Bonasoni, P.,
738 Vuillermoz, E., 2014. Implementation of a webGIS service platform for high

- 739 mountain climate research: the SHARE GeoNetwork project. *Geoscience Data*
740 *Journal* 1, 140–157. <https://doi.org/10.1002/gdj3.14>
- 741 MacDougall, A.H., Flowers, G.E., 2010. Spatial and Temporal Transferability of a
742 Distributed Energy-Balance Glacier Melt Model. *J. Climate* 24, 1480–1498.
743 <https://doi.org/10.1175/2010JCLI3821.1>
- 744 Meybeck, M., Green, P., Vörösmarty, C., 2001. A New Typology for Mountains and Other
745 Relief Classes. *mred* 21, 34–45. [https://doi.org/10.1659/0276-4741\(2001\)021\[0034:ANTFMA\]2.0.CO;2](https://doi.org/10.1659/0276-4741(2001)021[0034:ANTFMA]2.0.CO;2)
- 746 Miles, K.E., Hubbard, B., Quincey, D.J., Miles, E.S., Sherpa, T.C., Rowan, A.V., Doyle,
747 S.H., 2018. Polythermal structure of a Himalayan debris-covered glacier revealed by
748 borehole thermometry. *Scientific Reports* 8, 1–9. <https://doi.org/10.1038/s41598-018-34327-5>
- 749
750
- 751 Moore, G. w. k., Semple, J.L., 2009. The Impact of Global Warming on Mount Everest. *High*
752 *Altitude Medicine & Biology* 10, 383–385. <https://doi.org/10.1089/ham.2009.1039>
- 753 Moore, G.W.K., 2004. Mount Everest snow plume: A case study. *Geophysical Research*
754 *Letters* 31. <https://doi.org/10.1029/2004GL021046>
- 755 Moore, G.W.K., Semple, J.L., 2011. Freezing and frostbite on mount everest: new insights
756 into wind chill and freezing times at extreme altitude. *High Alt. Med. Biol.* 12, 271–
757 275. <https://doi.org/10.1089/ham.2011.0008>
- 758 Moore, G.W.K., Semple, J.L., 2006. Weather And Death On Mount Everest: An Analysis Of
759 The Into Thin Air Storm. *Bull. Amer. Meteor. Soc.* 87, 465–480.
760 <https://doi.org/10.1175/BAMS-87-4-465>
- 761 Moore, G.W.K., Semple, J.L., 2004. High Himalayan meteorology: Weather at the South Col
762 of Mount Everest. *Geophysical Research Letters* 31.
763 <https://doi.org/10.1029/2004GL020621>
- 764 Moore, K., Semple, J., Cristofanelli, P., Bonasoni, P., Stocchi, P., 2012a. Environmental
765 conditions at the South Col of Mount Everest and their impact on hypoxia and
766 hypothermia experienced by mountaineers. *Extrem Physiol Med* 1, 2.
767 <https://doi.org/10.1186/2046-7648-1-2>
- 768 Moore, K., Semple, J., Cristofanelli, P., Bonasoni, P., Stocchi, P., 2012b. Environmental
769 conditions at the South Col of Mount Everest and their impact on hypoxia and
770 hypothermia experienced by mountaineers. *Extreme Physiology & Medicine* 1, 2.
771 <https://doi.org/10.1186/2046-7648-1-2>
- 772 Mountain Research Initiative EDW Working Group, Pepin, N., Bradley, R.S., Diaz, H.F.,
773 Baraer, M., Caceres, E.B., Forsythe, N., Fowler, H., Greenwood, G., Hashmi, M.Z.,
774 Liu, X.D., Miller, J.R., Ning, L., Ohmura, A., Palazzi, E., Rangwala, I., Schöner, W.,
775 Severskiy, I., Shahgedanova, M., Wang, M.B., Williamson, S.N., Yang, D.Q., 2015.
776 Elevation-dependent warming in mountain regions of the world. *Nature Climate*
777 *Change* 5, 424–430. <https://doi.org/10.1038/nclimate2563>
- 778 Munro, D.S., 1990. Comparison of Melt Energy Computations and Ablatometer
779 Measurements on Melting Ice and Snow. *Arctic and Alpine Research* 22, 153–162.
780 <https://doi.org/10.1080/00040851.1990.12002777>
- 781 National Geographic, 2019. Perpetual Planet - Everest. URL
782 <https://www.nationalgeographic.org/projects/perpetual-planet/everest/> (accessed
783 3.27.20).
- 784 Oke, T.R., 2009. *Boundary Layer Climates*, Second. ed. Routledge.
- 785 Pellicciotti, F., Raschle, T., Huerlimann, T., Carenzo, M., Burlando, P., 2011. Transmission
786 of solar radiation through clouds on melting glaciers: a comparison of
787 parameterizations and their impact on melt modelling. *Journal of Glaciology* 57, 367–
788 381. <https://doi.org/10.3189/002214311796406013>

- 789 Pfeffer, W.T., Arendt, A.A., Bliss, A., Bolch, T., Cogley, J.G., Gardner, A.S., Hagen, J.-O.,
790 Hock, R., Kaser, G., Kienholz, C., Miles, E.S., Moholdt, G., Mölg, N., Paul, F.,
791 Radić, V., Rastner, P., Raup, B.H., Rich, J., Sharp, M.J., Consortium, T.R., 2014. The
792 Randolph Glacier Inventory: a globally complete inventory of glaciers. *Journal of*
793 *Glaciology* 60, 537–552. <https://doi.org/10.3189/2014JoG13J176>
- 794 Pokhrel, R., 2019. German, Spanish climbers eye toughest winter ascent on Mt Everest. *The*
795 *Himalayan Times*.
- 796 Pratap, B., Dobhal, D.P., Mehta, M., Bhambri, R., 2015. Influence of debris cover and
797 altitude on glacier surface melting: a case study on Dokriani Glacier, central
798 Himalaya, India. *Annals of Glaciology* 56, 9–16.
799 <https://doi.org/10.3189/2015AoG70A971>
- 800 Radić, V., Bliss, A., Beedlow, A.C., Hock, R., Miles, E., Cogley, J.G., 2014. Regional and
801 global projections of twenty-first century glacier mass changes in response to climate
802 scenarios from global climate models. *Clim Dyn* 42, 37–58.
803 <https://doi.org/10.1007/s00382-013-1719-7>
- 804 Rounce, D.R., King, O., McCarthy, M., Shean, D.E., Salerno, F., 2018. Quantifying Debris
805 Thickness of Debris-Covered Glaciers in the Everest Region of Nepal Through
806 Inversion of a Subdebris Melt Model. *Journal of Geophysical Research: Earth Surface*
807 123, 1094–1115. <https://doi.org/10.1029/2017JF004395>
- 808 Salerno, F., Guyennon, N., Thakuri, S., Viviano, G., Romano, E., Vuillermoz, E.,
809 Cristofanelli, P., Stocchi, P., Agrillo, G., Ma, Y., Tartari, G., 2015. Weak
810 precipitation, warm winters and springs impact glaciers of south slopes of Mt. Everest
811 (central Himalaya) in the last 2 decades (1994–2013). *The Cryosphere* 9, 1229–1247.
812 <https://doi.org/10.5194/tc-9-1229-2015>
- 813 Shea, J.M., Immerzeel, W.W., Wagnon, P., Vincent, C., Bajracharya, S., 2015. Modelling
814 glacier change in the Everest region, Nepal Himalaya. *The Cryosphere* 9, 1105–1128.
815 <https://doi.org/10.5194/tc-9-1105-2015>
- 816 Smith, A., Lott, N., Vose, R., 2011. The Integrated Surface Database: Recent Developments
817 and Partnerships. *Bull. Amer. Meteor. Soc.* 92, 704–708.
818 <https://doi.org/10.1175/2011BAMS3015.1>
- 819 Stigter, E.E., Litt, M., Steiner, J.F., Bonekamp, P.N.J., Shea, J.M., Bierkens, M.F.P.,
820 Immerzeel, W.W., 2018. The Importance of Snow Sublimation on a Himalayan
821 Glacier. *Front. Earth Sci.* 6. <https://doi.org/10.3389/feart.2018.00108>
- 822 Stull, R., 2015. *Practical Meteorology: An algebra-based survey of atmospheric science*,
823 First. ed. University of British Columbia.
- 824 Tonboe*, R.T., DybkjÆR, G., HØYer, J.L., 2011. Simulations of the snow covered sea ice
825 surface temperature and microwave effective temperature. *Tellus A: Dynamic*
826 *Meteorology and Oceanography* 63, 1028–1037. <https://doi.org/10.1111/j.1600-0870.2011.00530.x>
- 828 van den Broeke, M., van As, D., Reijmer, C., van de Wal, R., 2004. Assessing and Improving
829 the Quality of Unattended Radiation Observations in Antarctica. *J. Atmos. Oceanic*
830 *Technol.* 21, 1417–1431. [https://doi.org/10.1175/1520-0426\(2004\)021<1417:AAITQO>2.0.CO;2](https://doi.org/10.1175/1520-0426(2004)021<1417:AAITQO>2.0.CO;2)
- 832 Viviroli, D., Dürr, H.H., Messerli, B., Meybeck, M., Weingartner, R., 2007. Mountains of the
833 world, water towers for humanity: Typology, mapping, and global significance. *Water*
834 *Resources Research* 43. <https://doi.org/10.1029/2006WR005653>
- 835 Wang, S.-Y.S., Fosu, B., Giles, R.R., Singh, P.M., 2015. The deadly Himalayan snowstorm
836 of October 2014: synoptic conditions and associated trends [in “Explaining Extremes
837 of 2014 from a Climate Perspective”]. *Bulletin of the American Meteorological*
838 *Society* 96, S89–S94.

839 West, J.B., Boyer, S.J., Graber, D.J., Hackett, P.H., Maret, K.H., Milledge, J.S., Peters, R.M.,
840 Pizzo, C.J., Samaja, M., Sarnquist, F.H., et al., 1983. Maximal exercise at extreme
841 altitudes on Mount Everest. *Journal of Applied Physiology* 55, 688–698.
842 <https://doi.org/10.1152/jappl.1983.55.3.688>

843 Wheler, B.A., Flowers, G.E., 2011. Glacier subsurface heat-flux characterizations for energy-
844 balance modelling in the Donjek Range, southwest Yukon, Canada. *Journal of*
845 *Glaciology* 57, 121–133. <https://doi.org/10.3189/002214311795306709>

846 Wilby, R.L., Dawson, C.W., Murphy, C., O'Connor, P., Hawkins, E., 2014. The Statistical
847 DownScaling Model - Decision Centric (SDSM-DC): conceptual basis and
848 applications. *Climate Research* 61, 259–276. <https://doi.org/10.3354/cr01254>

849 Wild, M., Ohmura, A., Schär, C., Müller, G., Folini, D., Schwarz, M., Hakuba, M.Z.,
850 Sanchez-Lorenzo, A., 2017. The Global Energy Balance Archive (GEBA) version
851 2017: a database for worldwide measured surface energy fluxes. *Earth System*
852 *Science Data* 9, 601–613. <https://doi.org/10.5194/essd-9-601-2017>

853 Wilkinson, F., 2019. Traffic jams are just one of the problems facing climbers on Everest
854 [WWW Document]. Traffic jams are just one of the problems facing climbers on
855 Everest. URL [https://www.nationalgeographic.com/adventure/2019/05/everest-](https://www.nationalgeographic.com/adventure/2019/05/everest-season-deaths-controversy-crowding/)
856 [season-deaths-controversy-crowding/](https://www.nationalgeographic.com/adventure/2019/05/everest-season-deaths-controversy-crowding/) (accessed 11.30.19).

857 Wilks, D.S., 2011. *Statistical Methods in the Atmospheric Sciences*. Academic Press.

858 WMO, 2019. World Meteorological Organization's World Weather & Climate Extremes
859 Archive [WWW Document]. URL [https://wmo.asu.edu/content/world-](https://wmo.asu.edu/content/world-meteorological-organization-global-weather-climate-extremes-archive)
860 [meteorological-organization-global-weather-climate-extremes-archive](https://wmo.asu.edu/content/world-meteorological-organization-global-weather-climate-extremes-archive) (accessed
861 12.3.19).

862 Yang, X., Zhang, T., Qin, D., Kang, S., Qin, X., 2011. Characteristics and Changes in Air
863 Temperature and Glacier's Response on the North Slope of Mt. Qomolangma (Mt.
864 Everest). *Arctic, Antarctic, and Alpine Research* 43, 147–160.
865 <https://doi.org/10.1657/1938-4246-43.1.147>

866 You, Q.-L., Ren, G.-Y., Zhang, Y.-Q., Ren, Y.-Y., Sun, X.-B., Zhan, Y.-J., Shrestha, A.B.,
867 Krishnan, R., 2017. An overview of studies of observed climate change in the Hindu
868 Kush Himalayan (HKH) region. *Advances in Climate Change Research, Including*
869 *special issue on climate change in the Hindu Kush Himalaya* 8, 141–147.
870 <https://doi.org/10.1016/j.accre.2017.04.001>
871
872
873
874
875
876
877
878
879
880
881
882
883
884
885
886
887
888

889 **Tables**890 **Table 1.** AWS specifications for each of the 5 sites. Note that weights are only provided for

891 the highest stations which needed to be hand-carried to their install sites.

	Phortse	Base Camp	Camp II	South Col	Balcony
Latitude, longitude, and elevation	27.8456°N 86.7472°E 3810 m.a.s.l	27.9952°N 86.8406°E 5315 m.a.s.l	27.9810°N 86.9023°E 6464 m.a.s.l	27.9719°N 86.9295°E 7945 m m.a.s.l	27.9826°N 86.9292°E 8430 m.a.s.l
Operation	24/04/2019-present	10/10/2019-present	09/06/2019-present	22/05/2019-present	23/05/2019-present
Above ground sensor level (m)	2 m for temperature and humidity, 2.3 m for wind	2 m	2 m	1.5 m for temperature and humidity, 2m for wind	1.5 m for temperature and humidity, 2 m for wind
Air temperature sensor	Vaisala HMP155A-L5-PT; CS109	Vaisala HMP155A-L5-PT; CS109	Vaisala HMP155A-L5-PT; CS109	Vaisala HMP155A-L5-PT; CS109	Vaisala HMP155A-L5-PT; CS109
Relative humidity sensor	Vaisala HMP155A-L5-PT	Vaisala HMP155A-L5-PT	Vaisala HMP155A-L5-PT	Vaisala HMP155A-L5-PT	Vaisala HMP155A-L5-PT
Wind speed and direction sensor	R.M. Young 05108-45	R.M. Young 05108-45	R.M. Young 05108-45	2 × R.M. Young 05108-45	2 × R.M. Young 05108-45
Air pressure sensor	Vaisala PTB 110	Vaisala PTB210	Vaisala PTB210	Vaisala PTB210	Vaisala PTB210
Radiation sensor	2 × Hukseflux SR30 (up/down shortwave radiation); 2 × Hukseflux IR20 (up/down thermal radiation)	Hukseflux NR01	Apogee SN-500-SS	Hukseflux NR01	
Precipitation sensor	OTT Pluvio 2 and double alter shield	OTT Pluvio 2 and double alter shield	-	-	-
Present weather sensor	OTT Parsivel 2	OTT Parsivel 2	-	-	-
Relative surface elevation change sensor	Campbell Scientific SR50A	Campbell Scientific SR50A	Campbell Scientific SR50A	-	-
Data logger	Campbell Scientific CR1000X	Campbell Scientific CR1000X	Campbell Scientific CR1000X	Campbell Scientific CR1000X	Campbell Scientific CR1000X
Logger enclosure	Standard	Standard	Standard	Pelican case with military-spec quick-connects	Pelican case with military-spec quick-connects
Batteries	24 Ah	3 × 8Ah	3 × 8Ah	3 × 8Ah	3 × 8Ah
Charging	2 × 20W solar panels	2 × 20W solar panels	2 × 20W solar panels	2 × 10W solar panels	2 × 10W solar panels

Telemetry	Inmarsat	Thuraya; 400 MHz radio	Thuraya	Thuraya; 400 MHz radio	Thuraya; 400 MHz radio
Sampling interval	3 s (wind); 60 s (radiation, air pressure, temperature, relative humidity, precipitation) 3600 s (present weather, relative surface elevation change)	5 s (wind); 60 s (temperature, relative humidity, precipitation); 600 s (air pressure); 3600 s (present weather)	60 s (temperature, relative humidity, wind); 600 s (radiation); 3600 s (relative surface elevation change)	5 s (wind); 60 s (temperature, relative humidity, radiation); 600 s (pressure)	5 s (wind); 60 s (temperature, relative humidity); 600 s (pressure)
Tripod	Campbell Scientific CM106B	Campbell Scientific CM106B	Campbell Scientific CM106B	Custom Aluminum	Custom Aluminum
Approximate weight	Not available	Not available	Not available	Total: 50 kg Pelican case with logger: 8 kg Pelican case with batteries: 16 kg Tripod: 7 kg Crossarms, mounts, and bolts: 11 kg Sensors: 8 kg	Total: 50 kg Pelican case with logger: 8 kg Pelican case with batteries: 16 kg Tripod: 7 kg Crossarms, mounts, and bolts: 11 kg Sensors: 8 kg

892

893

894 **Table 2.** Comparison between monthly medians at the South Col from the new AWS (left-

895 hand columns, 2019 values) and those from the world's previous highest AWS at the South

896 Col (right-hand column, 2008 values) (Moore et al., 2012b).

	Air Pressure (hPa)		Air Temperature (°C)		Wind Speed (m s ⁻¹)	
	2019	2008	2019	2008	2019	2008
Jun	382.5	385.2	-14.2	-12.9	6.9	3.9
Jul	383.7	386	-11.7	-11.9	2.9	2.8
Aug	384.5	386.2	-13	-12.6	4.3	2.4
Sept	384.2	385.4	-14.7	-16.4	3.2	9.4
Oct	379.8	380.7	-21.7	-23	14.4	20

897

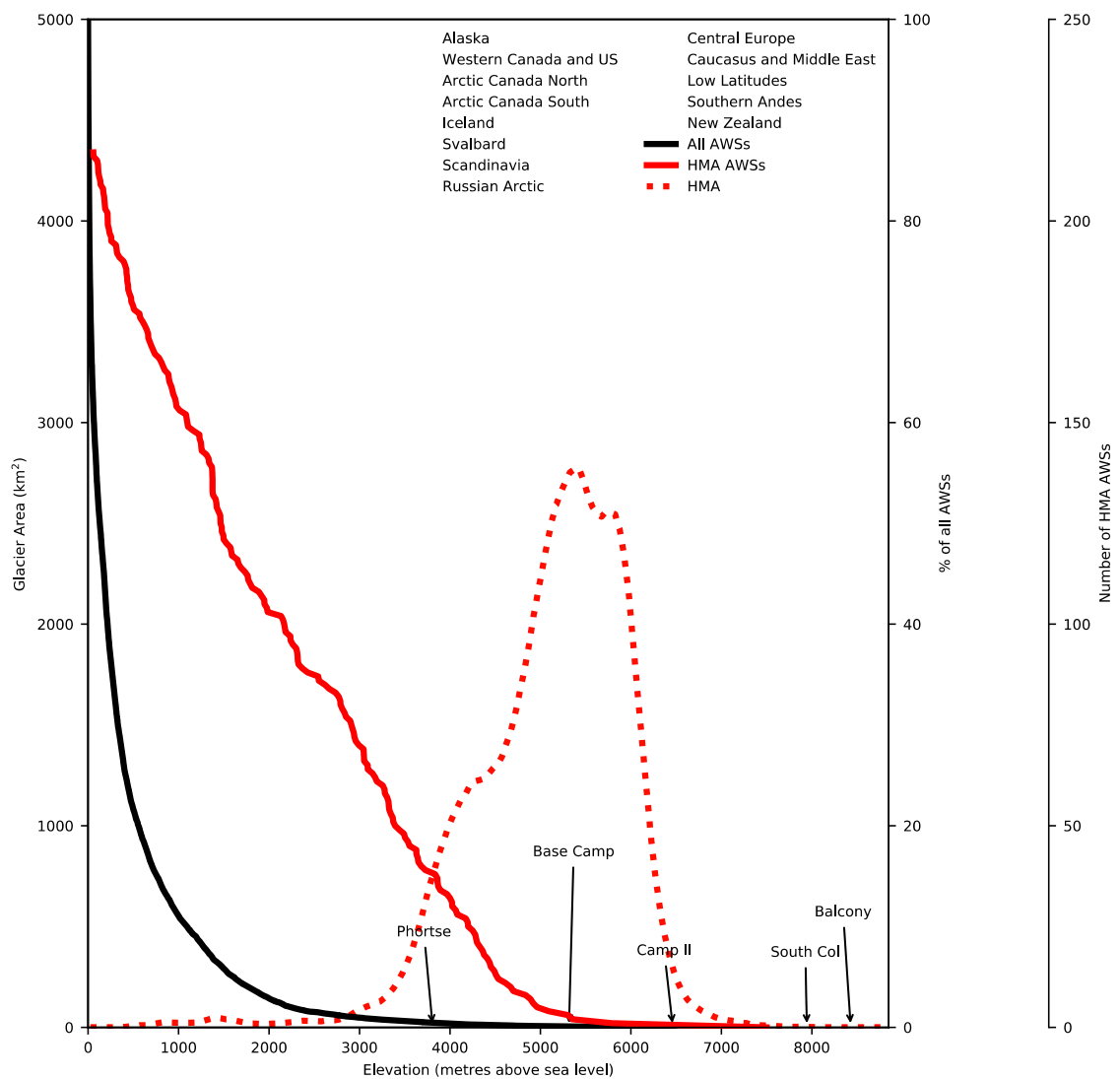
898 **Table 3.** Mean and standard deviation (of daily means) for the surface energy fluxes
 899 modelled for Camp II (6,464 m) and the South Col (7,945 m). See Eq. 1 and surrounding text
 900 for details of the notation used for the respective energy components.

Energy Flux	Camp II (W m^{-2})		South Col (W m^{-2})	
	Mean	Std. dev	Mean	Std. dev
Q_{SW}	57.6	16.2	65.2	17.4
Q_{LW}	-38.1	20.5	-49.4	24.9
Q_H	2.5	9.3	10.8	25.0
Q_L	--8.2	6.7	-25.2	13.2
Q_G	0.2	9.7	0.1	7.9
Q_M	14.0	14.3	1.4	4.4

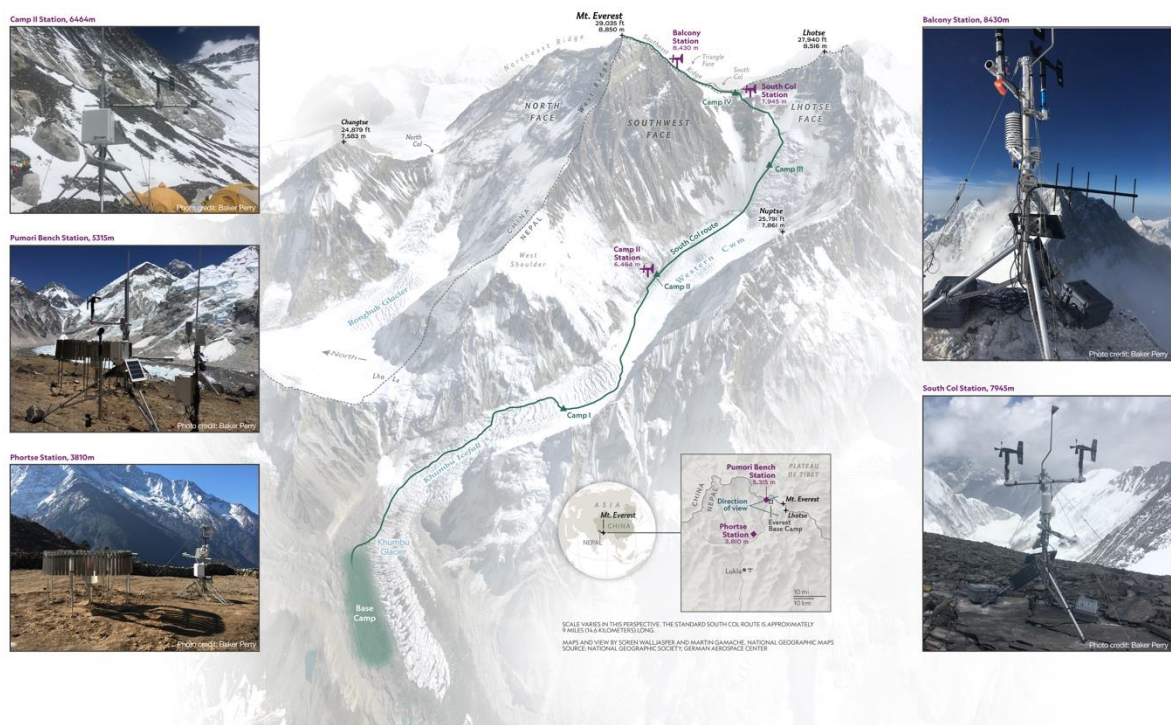
901
 902 **Table A1.** Mean meteorology estimated for the Summit (8,850 m) over the period 23 May—
 903 31 October 2019 and associated uncertainty, summarized as the median of all hourly estimates
 904 of uncertainty.

Variable [Units]	Mean	Uncertainty
Air temperature [$^{\circ}\text{C}$]	-20.6	2.1
Relative humidity [%]	63.7	23.0
Insolation [W m^{-2}]	349.1	79.4
Incident longwave radiation [W m^{-2}]	174.1	15.8

905
 906
 907
 908
 909
 910
 911
 912
 913
 914
 915
 916
 917



919 **Figure 1.** Percentage of all active AWSs above the elevation marked on the *x* axis, and the
 920 number of AWSs in High Mountain Asia (HMA) above the respective elevation, as identified
 921 from the Integrated Surface Database (Smith et al., 2011), with AWSs added from additional
 922 high-altitude networks known to the authors (see Appendix A). The elevations of the new
 923 AWSs from the 2019 Everest Expedition discussed in the text are annotated with arrows.
 924 Dotted/dashed lines give the glacier area-altitude distribution (hypsoetry) for all glacier
 925 regions in the Randolph Glacier inventory (Pfeffer et al., 2014), excluding Antarctica and
 926 Greenland. Note that the HMA curve is the sum of glacier areas in the Central Asia, South Asia
 927 West, and South Asia East regions.



929

930 **Fig. 2.** Map of locations referred to in the text. Also shown (inset) are photographs of the
 931 automatic weather stations installed during the 2019 Everest Expedition. Note the shovel
 932 handles used to mount the wind speed sensors on the Balcony weather station (upper right).

933

934

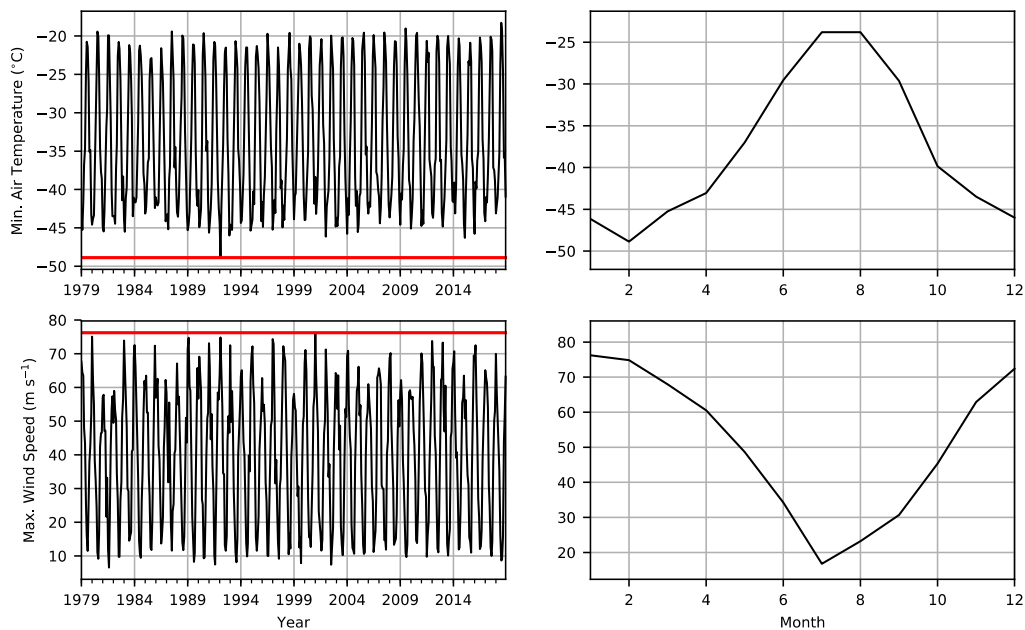
935

936

937

938

939



940

941 **Fig. 3.** Extreme temperatures and wind speeds in the ERA-Interim reanalysis at the summit of
 942 Everest (8,850 m.a.s.l), 1979-2018. Top left: Monthly time series of minimum temperature,
 943 with red line highlighting the all-time minimum (-49°C). Bottom left: Monthly time series of
 944 maximum wind speed (all-time maximum is 76 m s^{-1}). Top right: All-time minimum air
 945 temperature (line) in the reanalysis for the summit \pm one standard deviation of minima in that
 946 month across years. Bottom right: Same as top right but for maximum wind speeds.

947

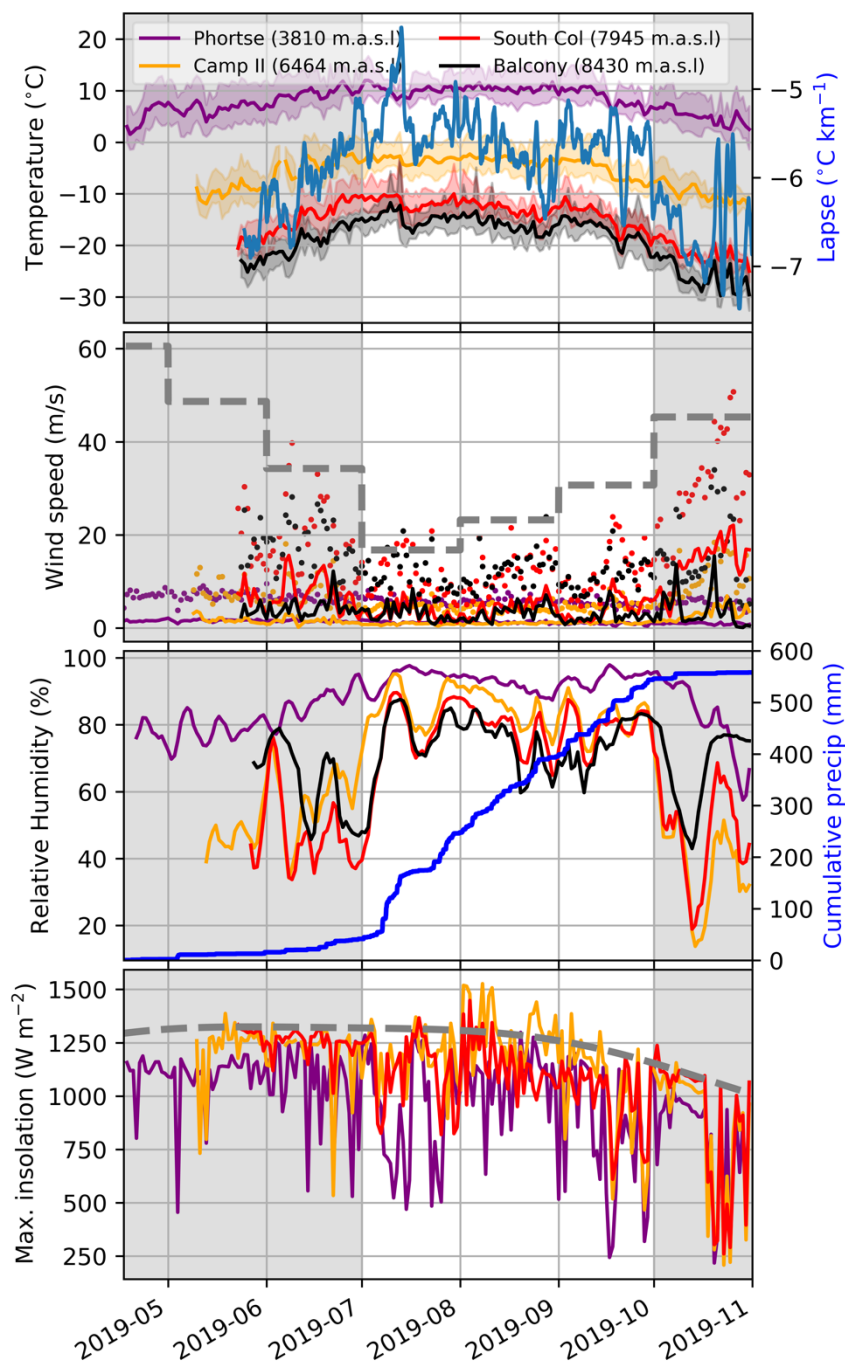
948

949

950

951

952

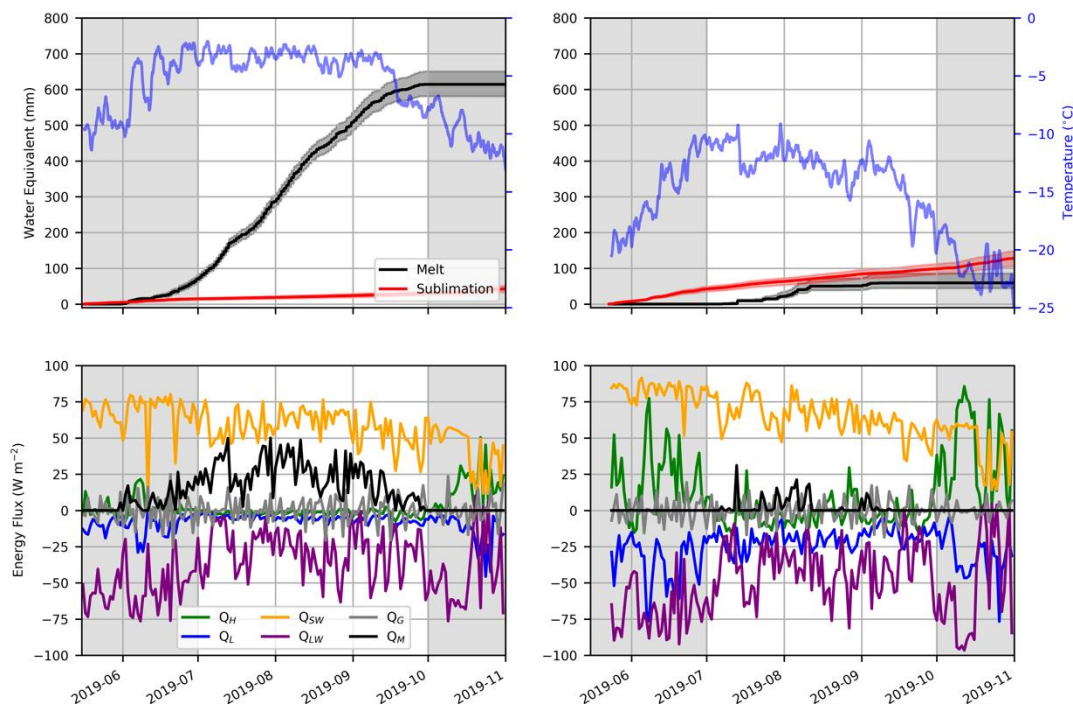


953

954 **Fig. 4.** Initial observations of selected variables at the AWSs. Top: Temperatures and lapse
 955 rates across all stations. Lapse rates were calculated as the slope coefficient from regressing
 956 running 24-hour mean air temperature at the AWSs against their elevations. Second top: Daily
 957 mean wind speeds (lines) and maximum gusts (points). The grey dotted line gives the all-time
 958 maximum wind speed in the ERA-Interim for the respective month. Second bottom: Mean

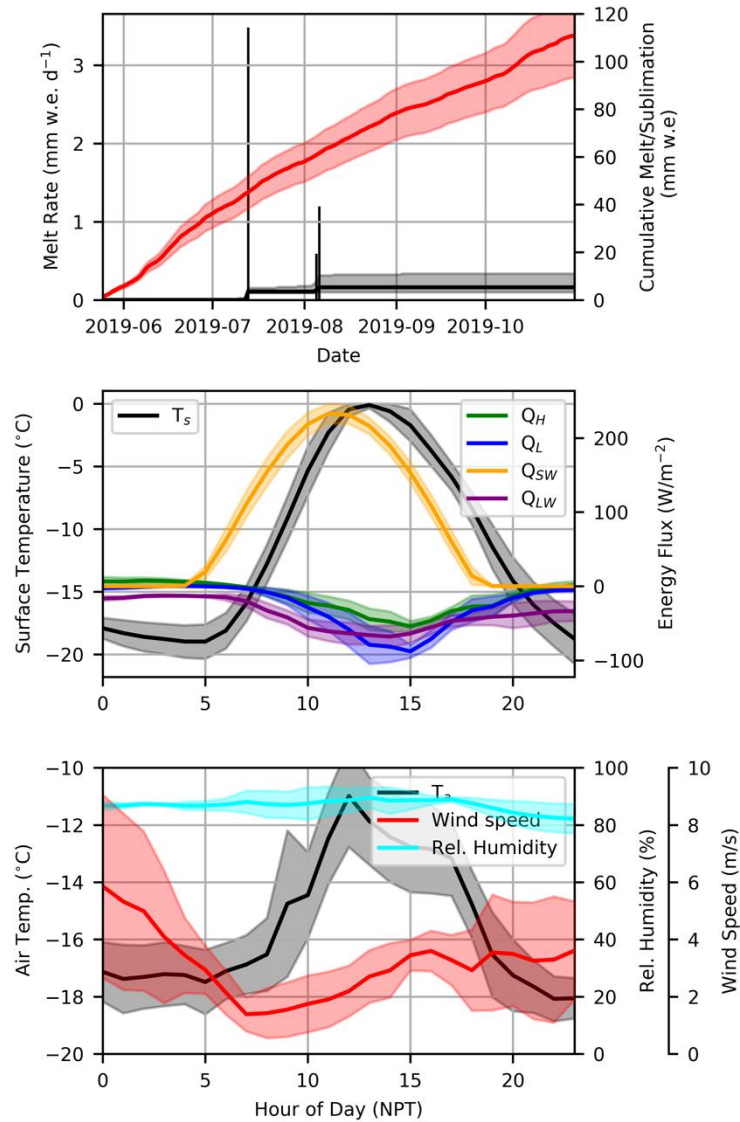
959 daily relative humidity smoothed with a three-day running mean. Cumulative precipitation at
 960 Phortse is plotted on the second (right) y-axis. Bottom: Daily maximum insolation at the AWSs
 961 (note that the Balcony site does not have a pyranometer). The grey dashed line here is the top-
 962 of-atmosphere incident flux, calculated using a solar constant of 1366 W m^{-2} and corrected for
 963 seasonal variations in Earth-sun distance. For all panels, the grey-shading highlights the non-
 964 monsoonal period.

965



966

967 **Fig. 5.** Simulated mass loss and energy fluxes at Camp II (left, 6,464 m) and the South Col
 968 (right, 7,945 m). Top row: Cumulative mass losses and daily mean air temperature, with shaded
 969 envelope spanning the daily minimum and maximum temperatures. The shaded envelope on
 970 the melt and sublimation curves indicates the uncertainty from perturbing the roughness length
 971 between the 5th and 95th percentiles of values reported in the literature for low-latitude snow-
 972 covered glaciers (see Appendix B). Bottom row: Mean daily energy fluxes, with notation
 973 consistent with Eq. 1.

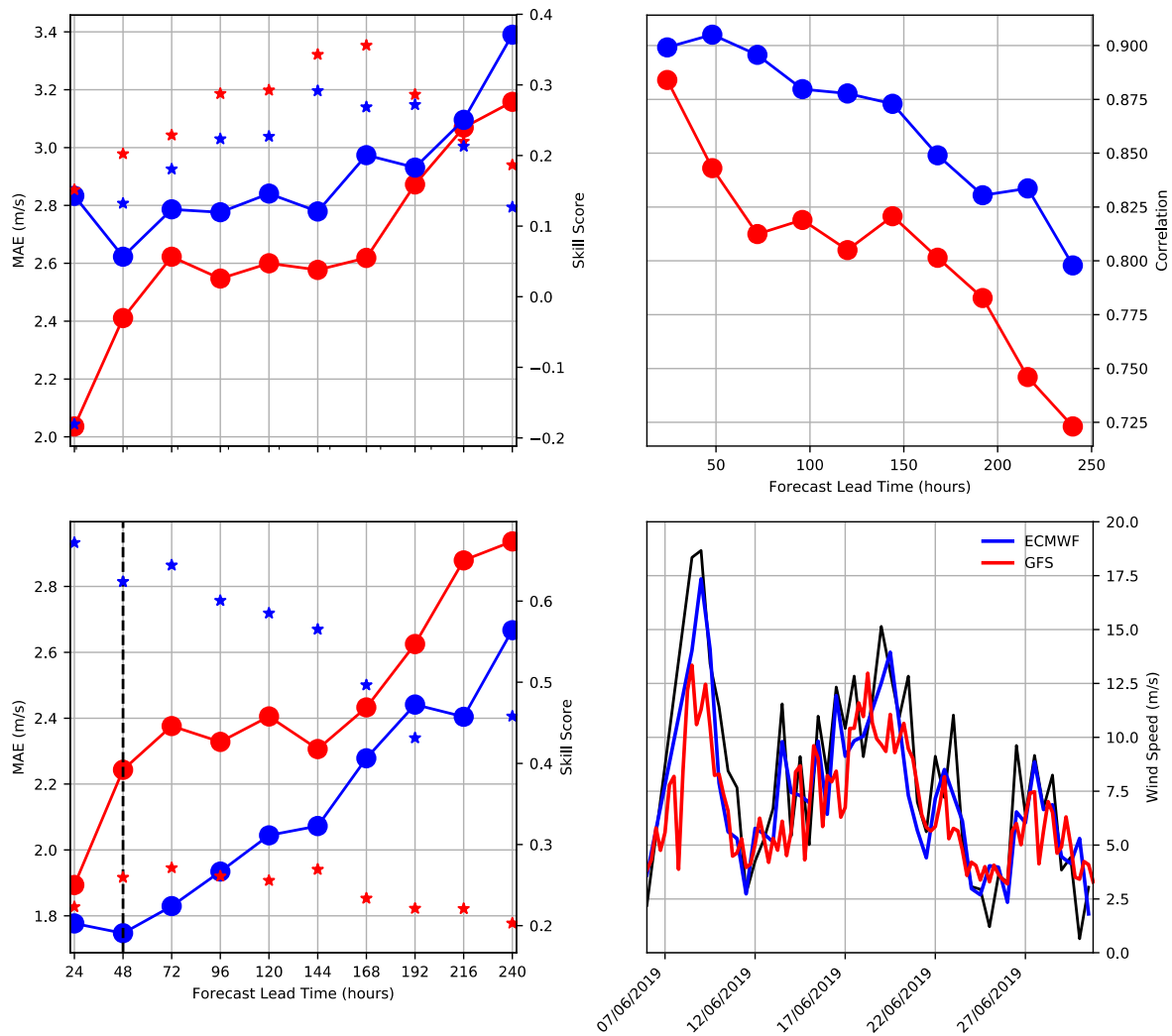


974

975 **Fig. 6.** Simulated mass losses, energy fluxes, and selected meteorological variables estimated
 976 for the summit. Top: Sublimation and melt, with the shaded envelope indicating the uncertainty
 977 from perturbing the roughness length (see Fig. 6 caption and Appendix B). Middle: Mean \pm
 978 standard deviation of energy fluxes and surface temperatures (T_s) as a function of hour of the
 979 day for all (four) days on which simulated melt for the summit was non-zero. Bottom: Same as
 980 middle but for selected meteorological variables.

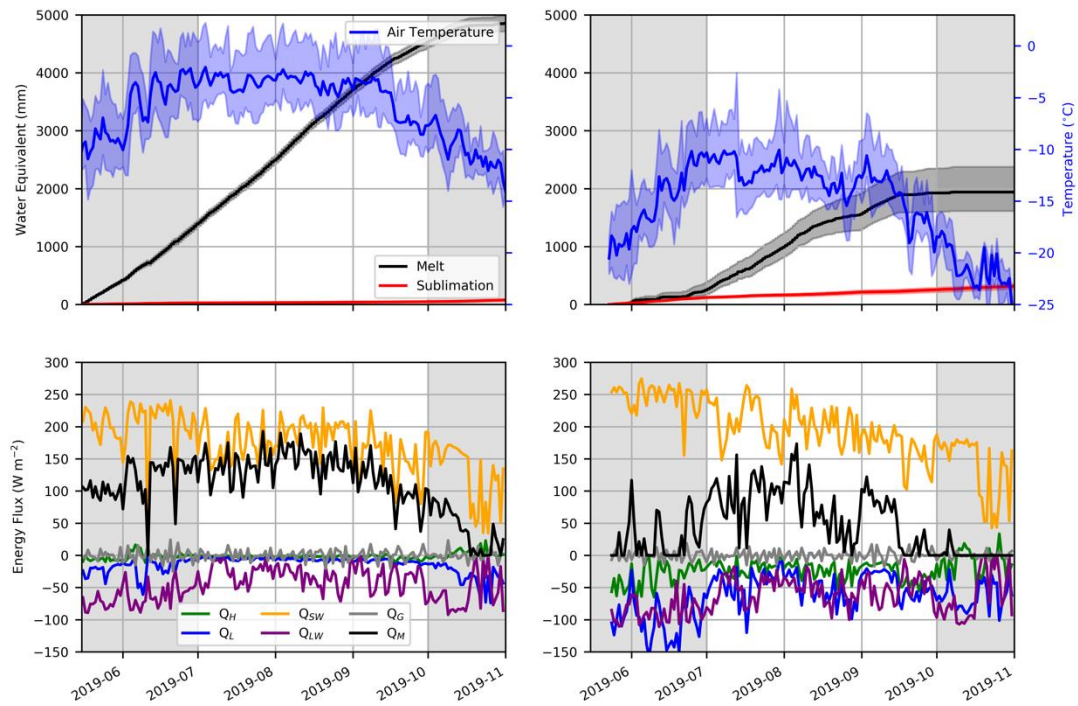
981

982



984

985 **Fig. 7.** Performance of the GFS and HRES wind speed forecasts at Everest's South Col (7,945
 986 m). Top left: MAE and skill scores (SS) as a function of lead time. Note that the skill score
 987 here is computed with a simple persistence forecast as the reference. Top right: Pearson
 988 product-moment correlation coefficients between observed and forecast hourly mean wind
 989 speed as a function of forecast lead time. Bottom left: As in top left, but for forecasts corrected
 990 with MOS. Here, the skill scores are computed for the MOS forecasts relative to the
 991 uncorrected forecasts. The vertical dotted line marks the performance at 48 hours; the forecast
 992 for this lead time is shown in the bottom right, during the pre-monsoon month of June 2019.



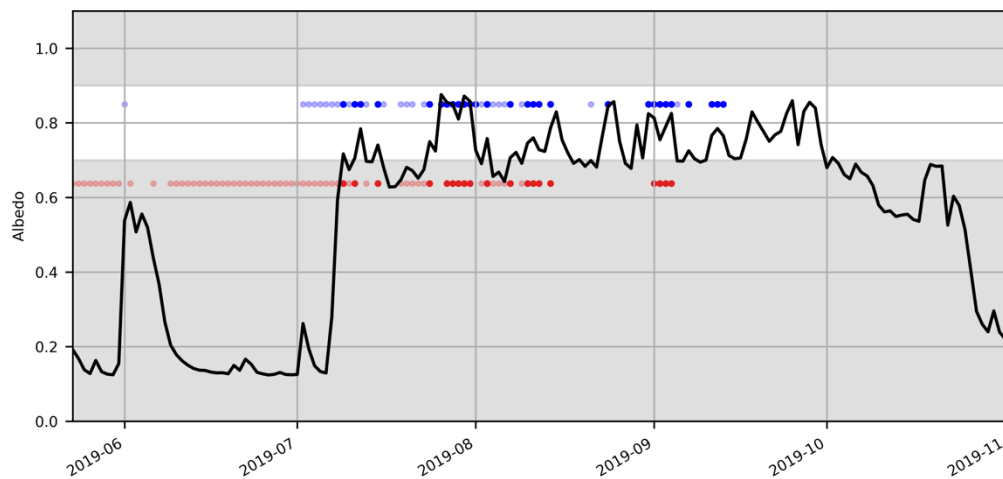
993

994 **Fig. A1.** As Fig. 4 in the main text, but for a hypothetical ice surface at Camp II (left panels)
 995 and the South Col (right panels), with albedo (α) set to 0.4 and near-surface density (ρ_s) of
 996 910 kg m^{-3} .



997
998
999

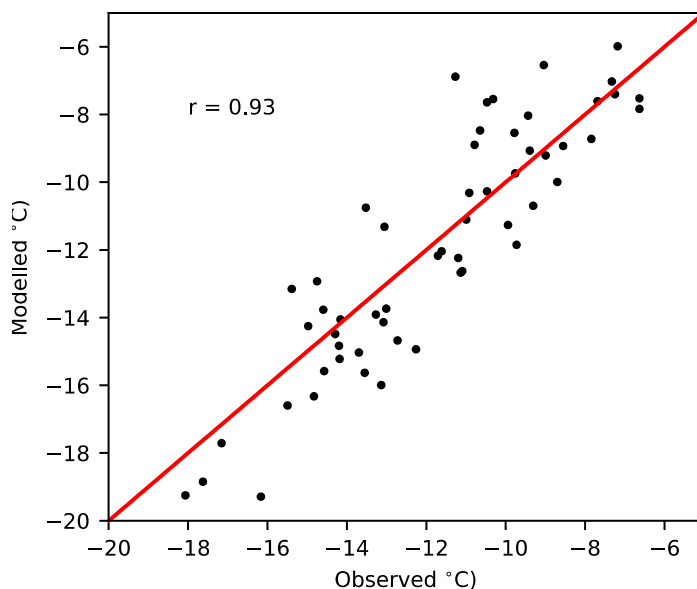
1000 **Fig. A2.** The South Col AWS being installed. Note the tents of Camp IV in the background,
1001 and the exposed glacier ice visible behind. Photo credit: Baker Perry / National Geographic.



1002
1003
1004

1005 **Fig. A3.** Albedo and possible melt events at the South Col AWS. Blue and red dots highlight those days on which melt was modelled (blue) and observed using the outgoing longwave heat

1006 flux (red). Bold indicates days on which the albedo was between 0.7 and 0.9, identifying
1007 periods of snow cover with an albedo similar to that used by the SEB model; values outside
1008 this range are masked with grey shading.



1009
1010 **Fig. A4.** Modelled and observed daily mean surface temperatures at the South Col during
1011 periods of fresh snow cover when the albedo was between 0.7 and 0.9. Note that observed
1012 surface temperature was inferred from the outgoing longwave heat flux (see text). The number
1013 annotated (r) indicates the (Pearson) correlation coefficient between the simulated and
1014 observed temperatures.
1015

1016
1017
1018
1019
1020
1021
1022